CHALMERS
UNIVERSITY OF TECHNOLOGY

Cooled Vane Heat Transfer

Master's Thesis in *Sustainable Energy Systems*

SANNA HOFFSTRÖM

Department of Applied Mechanics
CHALMERS UNIVERSITY OF TECHNOLOGY
Gothenburg, Sweden 2016

Master's Thesis 2016:32

Cooled Vane Heat Transfer

Sanna Hoffström

CHALMERS
UNIVERSITY OF TECHNOLOGY

Department of Applied Mechanics
Division of Fluid Dynamics
Chalmers University of Technology
Gothenburg, Sweden 2016

Cooled Vane Heat Transfer
Master's Thesis in *Sustainable Energy Systems*
Sanna Hoffström

Supervisors: Hans Abrahamsson, GKN Aerospace
Markus Olander Burak, GKN Aerospace
Examiner: Lars Davidson, Department of Applied Mechanics

Master's Thesis 2016:32
Department of Applied Mechanics
Division of Fluid Dynamics
Chalmers University of Technology
SE-412 96 Gothenburg
Telephone +46 31 772 1000

Typeset in LaTeX
Department of Applied Mechanics
Gothenburg, Sweden 2016

Cooled Vane Heat Transfer
Master's Thesis in Sustainable Energy Systems
Sanna Hoffström
Department of Applied Mechanics
Division of Fluid Dynamics
Chalmers University of Technology

Abstract

This Master's thesis project was carried out at the division of Engine Systems at GKN Aerospace, Trollhättan during the spring of 2016. In the project, jet impingement cooling with application to a cooled turbine inlet guide vane was studied with the purpose of developing and validating a model for the thermal load of the vane. As a start, a 2D model of a single slot jet was created and the predicted data compared to experimental data. This comparison showed that the choice of turbulence model highly influenced the results and variations of the $k-w$ model were considered most accurate. When extending this model to include a row of several jets, the assumption of a two-dimensional flow behaviour was found limiting. In the next step, a validation case of a single axisymmetric jet was performed. Area-average values of the differences between the predicted values and the experimental data used in the two validation cases were calculated and determined to maximally $\approx 15\%$. Based on findings from the two validation cases, a model of an array of circular jets was created.

Simulations with the jet array model showed that the jet inlet temperature was an acceptable choice of reference temperature. By comparing the results for models with two different jet inlet diameters it was found possible to assume a uniform behaviour of the non-dimensional parameters in the system when scaling up or down the system. Different heat transfer correlations for the heat transfer at the impingement surface were evaluated and some parameters could be singled out as especially important. This included the spacing between the inlets, whereas the effect of cross-flow in the array was considered minor. The evaluation indicated that it is possible to to estimate the thermal load by the use of heat transfer correlations if relevant parameters are included.

Keywords: Heat transfer coefficient, Nusselt number, jet impingement cooling, computational fluid dynamics, heat transfer correlations.

Nomenclature

Abbreviations

CAD	Computer-aided design
CFD	Computational fluid dynamics
RANS	Reynolds-averaged Navier–Stokes
SST	Shear stress transport

Greek symbols

Variable	Description	Unit
α	Correlation constant	–
β	Correlation constant	–
γ	Intermittency	–
ϵ	Turbulent dissipation	m^2/s^3
λ	Thermal conductivity	$W/(mK)$
μ	Dynamic viscosity	$kg/(ms)$
ρ	Density	kg/m^3
τ_{ij}	Stress tensor	Pa
ω	Specific rate of dissipation of turbulent kinetic energy	$1/s$

Roman symbols

Variable	Description	Unit
A	Area	m^2
B	Jet inlet width	m
C	Correlation constant	–
D	Jet inlet diameter	m
E	Total energy	J
f	Body forces	m/s^2
G_c	Cross-flow mass velocity based on channel cross-sectional area	kg/m^2s
G_j	Jet mass velocity based on jet hole area	kg/m^2s
H	Height	m
HTC	Local heat transfer coefficient	$W/(m^2K)$
$\overline{HTC}$	Area-averaged heat transfer coefficient	$W/(m^2K)$
$\overline{\overline{HTC}}$	Mean heat transfer coefficient	$W/(m^2K)$
h_n	Heat of formation for species n	J/kg
I	Turbulent intensity	–
j_n	Diffusional flux of species n	$mol/(m^2s)$
K_1, K_2	Correlation constants	–
k	Turbulent kinetic energy	m^2/s^2
L	Characteristic length	m
l	Turbulent length scale	m
m	Correlation constant	–
m_n	Mass fraction of species n	–

n	Correlation constant	–
n_x, n_y, n_z	Correlation constants	–
P	Pressure	Pa
q	Heat transfer rate	W
r	Jet inlet radius	m
S_E	Source of total energy	W
T	Temperature	K
t	Time	s
U	Instantaneous velocity	m/s
u	Fluctuating velocity	m/s
x_n	Streamwise jet hole spacing	m
y_n	Spanwise jet hole spacing	m
y^+	Non-dimensional distance from wall	–
$\langle U \rangle$	Mean velocity	m/s
$\langle u_i u_j \rangle$	Reynolds stress	m^2/s^2

Dimensionless numbers

Variable	Description	Definition
A_r	Ratio of the nozzle exit cross-sectional area to the surface area of the cell	$A_r = \frac{A_{c,e}}{A_{cell}}$
Nu	Nusselt number	$Nu = \frac{hL}{\lambda}$
Pr	Prandtl number	$Pr = \frac{C_p \mu}{\lambda}$
Re	Reynolds number	$Re = \frac{\rho L U}{\mu}$
$\widetilde{Re_{\theta t}}$	Transition onset momentum thickness Reynolds number	

Subscripts

c	Confinement
$cell$	Cell surface
c, e	Nozzle exit cross-sectional surface
in	Inlet
ref	Reference
w	Wall

Contents

1
Introduction

The performance and the efficiency of jet engines for aircraft propulsion have experienced a continuous improvement following their introduction in the mid 1940s. One factor that has played an important part in this development is the enabling of an increased turbine inlet temperature. When designing an engine that will operate at high temperature levels there are, however, thermal limitations of the material that need to be considered. Exposing the different components to high temperatures induces thermal stresses in the material that could reduce the lifespan of the engine and increase the risk of fatigue and failure [1]. A critical part of the engine is the guide vanes located at the inlet to the high-pressure turbine stage as these vanes receive the high-temperature gas flow leaving the combustor. To challenge these limitations and increase the thermal capability of the engine, different techniques for cooling of these vanes, both internally and externally, have been introduced.

The use of cooling, together with the development of improved materials, have allowed engine designers to continuously increase the turbine inlet temperature and by this improve the overall performance of the engines. Today, inlet temperatures exceeding the melting point of the materials are possible [2]. However, due to increasing fuel prices and more stringent regulations, the question of engine performance and efficiency is as prevalent as ever. As such, current research is aiming at increasing the turbine inlet temperature even further; something that will require a joint effort in developing new and improved materials and improving the effectiveness and the possibilities of turbine cooling.

1.1 Purpose and objective

GKN Aerospace is a global supplier of components and assemblies for aircraft application for both the civil and military market. The facility in Trollhättan is a part of the engine systems division that develops and manufactures components for jet and rocket engines, as well as stationary gas turbines. The extreme environments that these components need to withstand, along with the aviation industry's stringent safety regulations, place high demands on the design of the components. The ability to accurately predict and study the thermal load of different engine components is thus of high importance. Currently, a new thermal finite element (FE) model of

a cooled turbine guide vane is under development in Trollhättan and, within this work, the thermal load of the vane needs development and validation.

The inlet guide vane is cooled using both internal and external techniques; through jet impingement and film cooling, respectively. In this master's thesis project, a study of jet impingement and the corresponding heat transfer will be conducted with the purpose of developing and validating a model for the thermal load of the vane. In the study, different jet impingement configurations will be analysed; e.g. inlet type and hole spacing, together with the effect of varying the wall temperature at the impingement surface. The objective of the project is to develop heat transfer correlations for the cooled vane and provide a recommendation for the thermal modelling of the vane. More specifically, this means to:

- Study jet impingement cooling with application to the cooled vane.
- Evaluate and validate CFD simulations by comparison with experimental data.
- Use CFD to develop heat transfer correlations for the cooled vane.

1.2 Constraints

The project concerns the cooling of a single guide vane; however, only a fraction of the geometry is included in the different studies. The largest model include an array of eight jets and it is assumed that the jets are impinging perpendicularly on a flat surface, i.e. possible curvature of the vane is neglected. In the model for the jet array it is further assumed that the spacing between the jet inlets is uniform and that the configuration is staggered. Any roughness effects at the impingement surface are neglected and, furthermore, only steady-state analyses are performed.

2

Physical and theoretical background

This chapter will give an introduction to the physical and theoretical background of the project to make the reader familiar with key concepts and terms that are used in the thesis. In the first part, basic principles of fluid dynamics and heat transfer are introduced. Secondly, cornerstones of computational fluid dynamics (CFD) are presented along with principles of turbulence modelling. The last sections concern the need for turbine cooling in a gas turbine engine as well basic principles of jet impingement cooling and corresponding heat transfer correlations.

2.1 Fluid dynamics

A fluid is defined as a substance that deforms continuously when subjected to a shear stress. In the field of fluid dynamics it is typically the bulk behaviour of the fluid, rather than the behaviour on a molecular level, that is of interest. A common approach is thus to regard the fluid as a continuum; when in motion, the properties on a macroscopic level (or the bulk properties) of the continuum vary continuously within the fluid. The continuum approximation is valid whenever it is possible to determine relevant statistical averages of the fluid properties; the volume of interest thus need to be composed of a sufficient number of molecules for which the average values are determined [3]. Hereafter, when discussing properties of a fluid, it is the properties of the continuum that are intended.

Depending on its behaviour, a fluid flow can be classified as either laminar, turbulent or transitional. Turbulent flows are characterised by irregular and random fluctuations of the fluid properties in time and space; they are inherently chaotic. One factor that is used to describe this characteristic is the Reynolds number that represents the ratio of inertial to viscous forces in the flow. The Reynolds number is determined according to

$$Re = \frac{\rho L U}{\mu} \tag{2.1}$$

where ρ is the density of the fluid, L is the characteristic length of the system, U is the flow velocity, and μ is the dynamic viscosity of the fluid. Generally, a high Reynolds number is an indication of turbulence in the flow; at this point, the velocity

fluctuations in the flow have reached a level where they no longer can be dampened by the flow viscosity and the inertial forces become dominant [4].

2.2 Heat transfer principles

Heat transfer is the transport of thermal energy that occurs due to temperature gradients within or between different elements. There are three fundamental modes by which heat transfer is manifested: conduction, convection and radiation. The latter involves heat transfer in the form of electromagnetic waves, or photons, and is present in all systems where temperature gradients exist. The effect of radiation will, however, not be included in this project and as such, a presentation of the first two heat transfer processes, conduction and convection, is here given.

2.2.1 Conduction

There are two sources to conductive heat transfer: molecular interaction and movement of non-localised electrons within a medium. Molecular interaction involves heat transfer due to collisions of molecules with high energy content with less energetic ones; during the collisions heat (or kinetic and vibrational energy) is transferred in the direction of decreasing temperature. The effect of non-localised electrons on conductive heat transfer is primarily seen in pure metals where the ability of the material to conduct heat is directly related to the concentration of these electrons [3].

The rate of conductive heat transfer is determined according to the Fourier rate equation as

$$\frac{\mathbf{q}}{A} = -\lambda \, \nabla \mathbf{T} \tag{2.2}$$

where $\mathbf{q}$ is the conductive heat transfer rate, A is the area normal to the direction of heat transport, λ is the thermal conductivity of the material and $\nabla \mathbf{T}$ is the driving temperature gradient. The negative sign implies that heat is transferred from high temperature regions to regions with lower temperatures. The thermal conductivity is dependent on the structure and the composition of the material, as well as the temperature and the pressure [5].

2.2.2 Convection

Heat transfer between a surface and a neighbouring fluid, a process known as convection, is governed by two mechanisms. The first mechanism involves heat conduction and fluid motion in the near-wall region, whereas the second mechanism concerns motion of the bulk fluid. Depending on the source of fluid motion, convective heat transfer can be categorised as either natural or forced. In the case of natural convection, the motion of the fluid occurs due to heat conduction from the surface to an adjacent layer of stationary fluid. This heat conduction give rise to temperature gradients in the fluid that in turn cause the heated fluid parcels to expand and

displace. As the heated fluid displaces, it is replaced by fluid of a lower temperature, and a circulation phenomena occurs. Heat is thus, in addition to conduction, transported and spread by the motion of the fluid. Forced convection, on the other hand, involves fluid motion due to an external force that causes the fluid to mix. As a result, fluid regions with different temperatures are mixed and the heat transfer rate enhanced compared to natural convection [3].

It is the combined effect of heat conduction and fluid motion that determines the rate of convective heat transfer. This heat transfer rate is described by Newton's rate equation according to

$$\frac{q}{A} = HTC\ \Delta T \tag{2.3}$$

where q is the convective heat transfer rate, A is the surface area normal to the direction of the heat transport, ΔT is the driving temperature difference between surface and fluid and HTC is the convective heat transfer coefficient.

When studying convective heat transfer, the Nusselt number, describing the ratio between the convective thermal resistance and the conductive thermal resistance in the system, is commonly encountered. The Nusselt number is given as

$$Nu = \frac{HTC\ L}{\lambda} \tag{2.4}$$

where L is the characteristic length of the system, HTC is the convective heat transfer coefficient and λ is the thermal conductivity of the fluid.

2.3 Governing equations

Fluid motion and heat transfer are governed by conservation equations for mass, momentum and energy; here referred to as the *governing equations*. These equations, derived for a continuum, are coupled, partial and nonlinear differential equations that in the following sections are presented in a general form. It should be noted that the equations are given in tensor form and thus include an implicit summation of repeated indices.

2.3.1 Conservation of mass

Mass conservation in a system is described by the continuity equation that states mass can neither be destroyed nor created. The continuity equation is given by [4]

$$\frac{\partial \rho}{\partial t} + \frac{\partial (\rho U_i)}{\partial x_i} = 0 \tag{2.5}$$

where the first term describes the rate of mass accumulation and the second term the rate of convective mass transport in the system.

For an incompressible flow, having a constant density along a streamline, the continuity equation can be simplified to [4]

$$\frac{\partial U_i}{\partial x_i} = 0 \tag{2.6}$$

2.3.2 Conservation of momentum

The equation for conservation of momentum is based on Newton's second law of motion; stating that the force is equal to the mass times the acceleration. For a fluid element, the rate of change of momentum in a certain direction should thus be balanced by the net forces acting in the same direction. The forces that act on a fluid element are made up of body forces, such as the gravitational force, and surface forces due to normal and shear stress. With the assumption of an incompressible Newtonian fluid, for which a linear dependence exists between the shear stress and the rate of strain, the equations for conservation of momentum, one for each direction i, are given by the so called incompressible Navier-Stokes equations. These equations can be written on the form [3]

$$\rho\frac{\partial U_i}{\partial t} + \rho\frac{\partial (U_i U_j)}{\partial x_j} = -\frac{\partial P}{\partial x_i} + \mu\frac{\partial^2 U_i}{\partial x_j^2} + \rho f_i \tag{2.7}$$

In order of appearance, these terms represent the rate of accumulation, the transport by convection, the surface forces due to pressure distribution (normal stress), the viscous (or shear) stresses and the body forces acting on the element.

2.3.3 Conservation of energy

The first law of thermodynamics is based on the assumption of energy conservation; that energy can neither be destroyed nor created, it can only be transformed from one form to another. When applied to a fluid element, it states that the rate of change of energy of the fluid element is equal to the sum of the net rate of energy supplied to the element and the net rate of work done on the element by its surroundings. This requirement can be stated as a balance equation for total energy [4]

$$\frac{\partial E}{\partial t} = -\frac{\partial}{\partial x_j}\left[EU_j - \lambda\frac{\partial T}{\partial x_j} + \sum_n (m_n h_n j_n) - \tau_{ij} U_i\right] + S_E \tag{2.8}$$

where the total energy, E, is the sum of kinetic, thermal, chemical and potential energy in the system. The terms in the energy equation represent accumulation, convective transport, conductive transport, diffusional transport, viscous dissipation and source term.

2.4 Turbulence modelling

Turbulent flows are characterised by small-scaled, high-frequency fluctuations of the instantaneous flow properties, e.g. the velocity components and the pressure. To

resolve these fluctuations and describe the flow completely would require a huge amount of data and computational effort. To overcome these requirements, the governing equations are manipulated to remove these fluctuations and only a time-averaged form of the equations governing the mean flow are solved. A common way of doing this is to decompose the instantaneous variables into a mean and a fluctuating part; a procedure known as Reynolds decomposition. For the velocity, this decomposition gives

$$U_i = \langle U_i \rangle + u_i \tag{2.9}$$

where U_i represents the instantaneous value, $\langle U_i \rangle$ the mean and u_i the fluctuating part of the velocity. By inserting the expression for the decomposed variables in the governing equations introduced above and taking the time-average the equations, the equations for conservation of mass and momentum are reduced to

$$\frac{\partial \langle U_i \rangle}{\partial x_i} = 0 \tag{2.10}$$

$$\frac{\partial \langle U_i \rangle}{\partial t} + \langle U_j \rangle \frac{\partial \langle U_i \rangle}{\partial x_j} = -\frac{1}{\rho}\frac{\partial \langle P \rangle}{\partial x_i} + \frac{\mu}{\rho}\frac{\partial^2 \langle U_i \rangle}{\partial x_j^2} - \frac{\partial \langle u_i u_j \rangle}{\partial x_j} \tag{2.11}$$

This form of the Navier-Stokes equation are called the Reynolds-averaged Navier-Stokes equations, or simply the RANS equations. As a consequence of the time-averaging procedure, new unknown terms, $\langle u_i u_j \rangle$, or in the form of a stress tensor $-\rho\langle u_i u_j \rangle$, called the Reynolds stresses, are introduced in the RANS equations. As the system of equations now contains more unknowns than the total number of equations, turbulence models are needed in order to determine the Reynolds stresses and close the equation system.

There are today several options available for modelling of the Reynolds stresses and many of these are based on an approximation called the Boussinesq approximation. This approximation assumes that the components of the Reynolds stress tensor are proportional to the mean velocity gradients and that the turbulent momentum transport can be modelled using a turbulent viscosity. Turbulence models based on this approximation include an additional number of transport equations describing the turbulent length and velocity scales; these additional equations are solved together with the RANS equations to determine the turbulent viscosity. Depending on the number of additional transport equations that are solved, turbulence models can be categorised as e.g. zero-, one- or two-equation models. By using two-equation models, it is possible to determine the turbulent length and velocity scales independently; these models are sometimes called complete models.

Two commonly used two-equation models are the $k-\epsilon$ and the $k-\omega$ model. In the $k-\epsilon$ model, transport equations for the turbulent kinetic energy, k, and the turbulent dissipation, ϵ, are used to determine the turbulent velocity and length scales in the system. In the $k-\omega$ model, the specific rate of dissipation, ω, is instead used for prediction of the length scale [4]. The standard $k-\epsilon$ model is widely used for high Reynolds flows; however, for prediction in low Reynolds regions, it requires modification in terms of dampening functions or to be used in combination with

wall functions. With the $k-\omega$ model it is possible to apply the model directly for near-wall predictions; this, however, requires a very fine mesh resolution close to the wall [6].

From these models, alternative turbulence models have been developed. One example is the realizable $k-\epsilon$ model that includes a constraint for the normal Reynolds stress term, ensuring that this term remains positive for all types of flows. Without this constraint, as in the standard $k-\epsilon$ model, problems with realizability could arise when modelling flows with large normal stresses [4]. Another example is the SST (shear stress transport) $k-\omega$ model that is based on a combination of the standard $k-\omega$ model and the standard $k-\epsilon$ model; it uses the $k-\omega$ formulation for prediction in the near-wall region and the k-ϵ formulation for prediction in the free stream. This makes it possible to apply the model directly for near-wall predictions, and by switching to the $k-\epsilon$ formulation in the outer regions, it becomes less sensitive to free-stream turbulence properties [6]. In the commercial CFD-software ANSYS Fluent, it is possible to enable a low Reynolds correction for the SST $k-\omega$ model. This correction is in the form of a dampening constant in the function for determining the turbulent viscosity. This software also provides the opportunity of using of a SST transition model. The SST transition model combines transport equations for k and ω with transport equations for intermittency, γ, and a transition onset criteria (in terms of a transition momentum thickness Reynolds number), $\widetilde{Re_{\theta t}}$ [7].

2.5 Engine performance and the need for cooling

The basic principle of a jet engine, as shown in Figure 2.1, can be described with a simple gas turbine cycle using three processes; compression, combustion and expansion. In the first step, the pressure of the intake air from the fan is increased to a high pressure level by a compressor. This is followed by mixing and combustion of the pressurised air with the fuel to produce a high-temperature gas. The gas is then expanded in a turbine where kinetic energy is extracted from the gas flow and converted into mechanical energy, or shaft power, that drives the compressor. As a last step, a nozzle is used to generate thrust for the aircraft by accelerating the gas flow further [1].

The specific thrust and the specific fuel consumption of the gas turbine cycle is directly benefited by a high turbine inlet temperature and modern jet engines normally operate at very high temperature levels. For a given pressure ratio, a high turbine inlet temperature is also favorable when trying to obtain a high thermal efficiency of the cycle [9]. The possibility of increasing the turbine inlet temperature is, however, limited by the maximum temperature that the material in the subsequent parts of the engine can withstand. When attempting to increase this temperature level, the thermal capability of the turbine guide vanes is thus critical. High temperature levels and gradients within the vanes could induce thermal stresses, oxidation and creep that limit the lifetime of the engine and increase the risk of fatigue and failure [1].

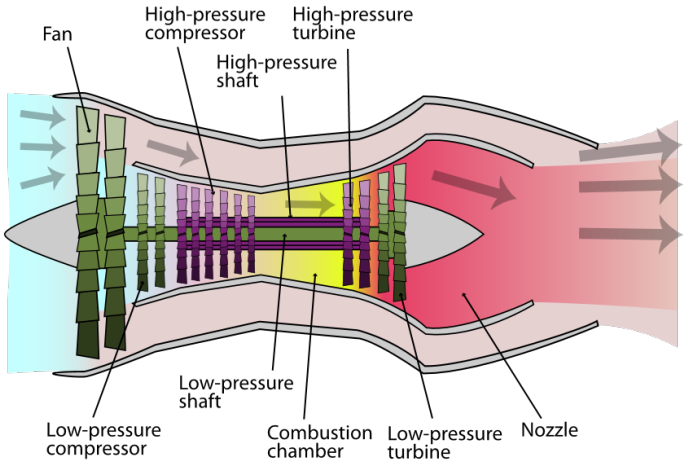

Figure 2.1: Schematic illustration of a 2-spool, low-bypass turbofan engine [8].

To ensure safe operation at these high temperature levels, different techniques for cooling of the vanes are applied; today, a combination of both internal and external cooling techniques can be used. External cooling involves the use of film cooling at the vane's outer surface, whereas internal cooling is achieved by a combination of convection and jet impingement cooling. With jet impingement cooling it is possible to obtain high heat transfer coefficients and a more thorough explanation of the physics and behaviour of jet impingement cooling is given in the following section.

2.6 Jet impingement cooling

Due to requirements on the surrounding structures, jet impingement cooling is commonly only used for cooling of selected parts of the engine that are exposed to very high thermal loads such as the leading edge and mid-chord of turbine guide vanes. An illustration of a typical cooled first stage turbine inlet guide vane is shown in Figure 2.2. Jet impingement cooling utilises pressurised cooling air, bled from the compressor stage, as a cooling source. The pressurised air is passed through small holes in the surface of perforated inserts, placed inside the internal cavities of the vane. When the air exits these holes, it forms high velocity jets that impinge on the inside of the wall of the vane transferring heat from the surface. The spent air leaves through cooling holes in the external wall, providing an additional cooling effect in the form of film cooling, or at the trailing edge before it mixes with the gas flow in the main stream [10].

There are several factors that determine the behaviour of an impinging jet, and thereby also the effectiveness of jet impingement cooling. Firstly, a distinction should be made between different types of inlets, or nozzles, that can be applied. Typically, either a slot jet, with a relatively uniform velocity profile, or a round jet, with an axisymmetric velocity profile is used [11]. In a turbine guide vane, an array of confined round jets is obtained from the perforated inserts placed inside the vane's cavities. Another important geometrical factor is the distance between

the jet inlet and the target surface. This distance is often defined in dimensionless form as H/D, where H is the distance between the jet inlet and the target surface and D is the jet inlet diameter; in the case of a slot jet, the width of the inlet, B, is taken as the denominator. One important fluid parameter is the impinging jet Reynolds number. Herein, the jet Reynolds number is determined according to eq. 2.1 with the inlet diameter, or width, as characteristic length and the velocity, as well as the fluid properties, evaluated at the jet inlet. Furthermore, when studying jet impingement cooling in a guide vane, there are additional effects of e.g. jet inlet hole configuration (staggered or in-line), spacing between the inlets, and cross-flow due to upstream jets to consider.

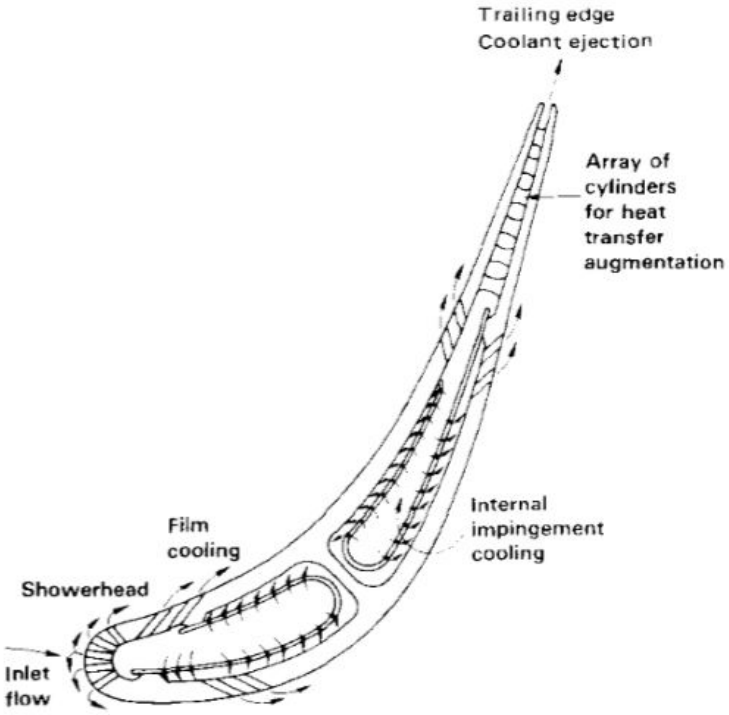

Figure 2.2: Illustration of a cooled first stage turbine inlet guide vane [12].

2.6.1 Physics of a single jet

After exiting the nozzle, an impinging jet demonstrates a flow field characterised by three distinct regions; an illustration of these different regions is shown in Figure 2.3. At a distance sufficiently far from the impingement surface the jet is unaffected by the presence of the surface and behaves as a free jet. This region is thus called the *free jet region*. Here, the jet consists of two sub-regions; the *shear layer* and the *potential core*. The shear layer is characterised by an interaction between the jet and the surrounding fluid caused by velocity gradients between the two. The presence of velocity gradients causes a shearing at the edges of the jet, resulting in entrainment of surrounding fluid that increases the jet diameter and the mass flow of the jet. In the potential core, the jet velocity is conserved and thus equal to the condition at the jet inlet.

When approaching the impingement surface, the velocity of the jet is reduced until the flow is forced to change direction. This deceleration region is called the *stagnation region*. At the center of the stagnation region, where the local velocity of the fluid is zero, the boundary layer is relatively thin and the heat transfer rate enhanced; this point is called the *stagnation point*. At very small H/D, the build up of static pressure in the stagnation region could influence the behaviour of the upstream jet in the region close to the jet inlet. In such case, a free jet region may not exist. After exiting the stagnation region, the jet spreads further outward into the *wall jet region* as the distance, x/D (slot jet) or r/D (circular jet), from the stagnation point increases. In this region, the heat transfer is governed by the boundary layer that develops on the impingement surface [11].

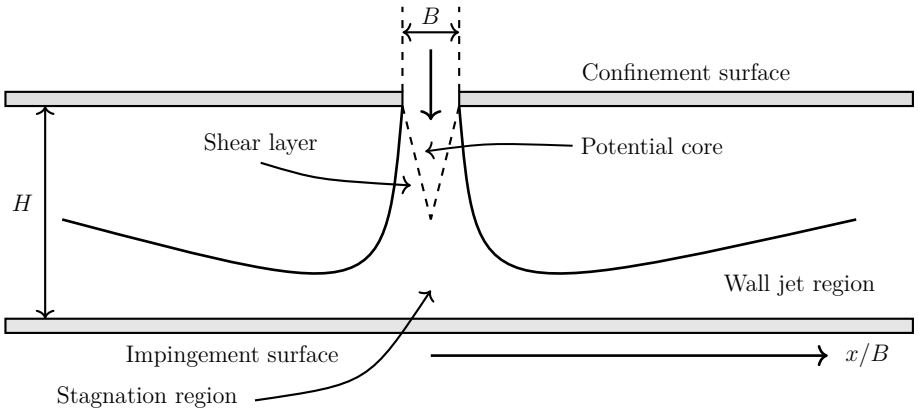

Figure 2.3: Illustration of different jet regions for a single impinging slot jet.

The resulting heat transfer at the impingement surface can be evaluated by studying either the convective heat transfer coefficient or the corresponding Nusselt number. The heat transfer coefficient is determined by Newton's rate equation, given by eq. 2.3. The driving temperature difference is normally taken as the difference between jet inlet temperature, T_{in}, and a reference temperature (commonly the temperature of the impingement surface, T_w). The Nusselt number for impingement cooling, given by eq. 2.4, is determined from the convective heat transfer coefficient together with the inlet diameter, or width, and the thermal conductivity of the fluid, evaluated at the reference point [11].

2.6.2 Heat transfer correlations

Another way of estimating Nusselt numbers is through the use of heat transfer correlations. Existing correlations have commonly been developed empirically, by fitting experimental data to an expected function. For forced convection problems, the Nusselt number is typically given as a function of the Reynolds number and the Prandtl number, i.e. $Nu = f(Re, Pr)$. Depending on the type of geometry that is studied, the correlations can be extended to also include the effect of different geometrical parameters. In the review article "*Heat and mass transfer between impinging gas jets and solid surfaces*" [13], Martin recommends a correlation of the

form $Nu = f(Re, Pr, r/D, H/D)$ for an array of staggered jets. In Appendix A, the parameter intervals for which the correlation is valid are presented. In its complete form, the correlation is given as

$$Nu = K\left(A_r, \frac{H}{D}\right)G\left(A_r, \frac{H}{D}\right)F(Re)Pr^{0.42} \tag{2.12}$$

The K and G are geometrical parameters of the domain and are determined according to

$$K = \left[1 + \left(\frac{H/D}{0.6/A_r^{1/2}}\right)^6\right]^{-0.05} \tag{2.13}$$

$$G = 2A_r^{1/2}\left[\frac{1 - 2.2A_r^{1/2}}{1 + 0.2(H/D - 6)A_r^{1/2}}\right] \tag{2.14}$$

where the constant A_r is the ratio of the nozzle exit cross-sectional area, $A_{c,e}$, to the surface area of the cell, A_{cell}. An illustration showing the definition of these parameters can be seen in Figure 2.4. The variable H/D is the non-dimensional nozzle-to-wall spacing introduced in Section 2.6.

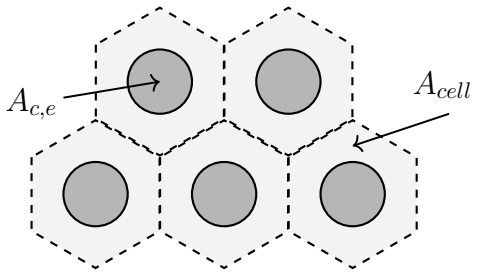

Figure 2.4: Illustration of nozzle exit cross-sectional area, $A_{c,e}$, and cell surface area, A_{cell}, for an array of staggered circular jets.

Lastly, the variable F is a function of the Reynolds number given as

$$F = 0.5Re^{2/3} \tag{2.15}$$

Another attempt of describing experimental data for an array of circular jets with a function for the Nusselt number was conducted by Florschuetz et al. [14]. They found that, except for geometrical parameters, the crossflow from upstream jets influenced the heat transfer of the impinging jets. They developed a correlation of the form

$$Nu = K_1 Re^m\left(1 - K_2\left[\left(\frac{H}{D}\right)\left(\frac{G_c}{G_j}\right)\right]^n\right)Pr^{1/3} \tag{2.16}$$

where the effect of crossflow is incorporated in the ratio of the crossflow mass velocity based on the channel cross-sectional area, G_c, and the jet mass velocity based on the jet hole area, G_j.

The coefficients K_1 and K_2, as well as the exponents m and n, depend on the streamwise jet hole spacing, x_n, and the spanwise jet hole spacing, y_n, together with the non-dimensional nozzle-to-wall spacing, H/D. This dependency is given by

$$K_1, K_2, m, n = C\left(\frac{x_n}{D}\right)^{n_x}\left(\frac{y_n}{D}\right)^{n_y}\left(\frac{H}{D}\right)^{n_z} \tag{2.17}$$

where the values of the exponents n_x, n_y and n_z, and the constant C, are specified separately for each individual constant, i.e. for K_1, K_2, m and n; these values can be found in Table A.1 in Appendix A.

3
Methodology

The first part of this chapter will provide an insight to the general procedure and approach that was used when performing CFD simulations throughout the project. In the second part of the chapter, a presentation of the different cases that were studied will be given.

3.1 Procedure and approach

When performing CFD simulations and analyses for the different cases included in the project, a general procedure and approach was used. This included geometry definition, mesh generation, specification of boundary and initial conditions, model definition, settings for properties, solver settings and solution. In the following sections, these different parts of the project are described in more detail.

3.1.1 Geometry and mesh generation

As a first step, a model of the geometry was constructed using the computer-aided design (CAD) system ANSYS DesignModeler; in all models it was assumed that the jets impinged perpendicularly on a flat surface. To reduce the computational effort required for performing the simulations, only a part of the real geometry was modelled and the geometries were simplified by applying mirror symmetry or translational periodicity. When constructing the CAD model, the geometry was divided into sub-domains to ease the control of mesh size in different regions of the domain.

The finished CAD model was exported to ANSYS Meshing where a mesh was generated for the domain. The density of the mesh was distributed so that a finer mesh was used in the regions corresponding to the expected free jet and stagnation region as well as in the near-wall region. This was done to accurately resolve velocity gradients and shearing between the jet and the ambient fluid together with both thermal and velocity boundary layers at the impingement surface. At the impingement surface, the first layer height of the cells where set so that a value of $y^+ < 1$ was obtained for the entire surface. For the free stream closer to the outlet of the domain, where the flow is aligned with the cells, a coarser mesh was used.

3.1.2 Boundary and initial conditions conditions

A uniform velocity profile was used as inlet condition in the majority of the simulations and either a velocity magnitude or a mass flow was given together with the direction of the flow. The turbulent flow variables were specified by setting a turbulent intensity together with either a viscosity ratio or a turbulent length scale. However, in the case of a single axisymmetric jet, a fully developed profile was desired at the jet inlet. In this case, the inlet boundary conditions were iterated until a fully developed profile was obtained. This profile, containing the velocity in x-, y- and z-direction together with the turbulent kinetic energy and the specific dissipation rate, was then used for defining the inlet conditions for the domain. In all models, the outlet was specified as a pressure outlet and the outlet gauge pressure was set so that a desired total pressure at the inlet was obtained. For the walls, a no slip condition was specified and the thermal condition was given as a constant wall temperature. Based on these simulation settings, a hybrid initialisation was performed to provide an initial guess for the simulation.

3.1.3 Model definition and properties

The flow field and heat transfer were modeled based on the RANS equations for conservation of mass and momentum (described in Section 2.4) together with the equation for energy conservation. To close the equation systems, a turbulence model was chosen. Validation cases were performed where different turbulence models were tested and evaluated based on comparison with experimental data. From the evaluation, one turbulence model was chosen and used in the subsequent simulations.

At a lower temperature range, the properties of the fluid, i.e. specific heat capacity, thermal conductivity and dynamic viscosity, were calculated using ANSYS Fluent's built-in piecewise-linear function and data for the relevant temperature range. At higher temperature ranges, corresponding to those encountered in a typical engine, a user-defined function was provided to perform these calculations.

3.1.4 Solver settings and solution

To perform the simulations, the CFD software ANSYS Fluent 16.0 was chosen. A pressure-based solver was employed and the coupled scheme was used for the pressure-velocity coupling. If no other information is given, the second order upwind scheme was used for spatial discretization of all terms in the final simulations and, as the flow was assumed to be steady in time, no temporal discretization was used. During the simulations, the progression of heat transfer coefficients, outlet mass flow and flow variables (outlet temperature and pressure) were monitored and the simulations were run until these variables had stabilised. For the solution to be considered converged, oscillations with small amplitudes, corresponding to a maximum deviation between the iteration values of approximately one percent, could be accepted. For each model, the heat flux at the impingement surface was used to determine corresponding heat transfer coefficients and Nusselt numbers using eq. 2.3 and eq. 2.4, respectively.

3.2 Description of cases

As a start, simulations were performed for a model of a single impinging slot jet. The model was constructed in 2D and by comparing the Nusselt numbers predicted by the CFD simulations with experimental data, the choice of turbulence model was validated. A mesh study was performed for this model and the outcome from this study was used as a basis for constructing meshes for the subsequent cases. In the next step, the model of a single slot jet was extended to include a row of impinging jets. The second part of the project concerned modelling of circular impinging jets; these models were thus constructed in 3D. Firstly, a validation case for a single axisymmetric jet was performed to evaluate the performance of different turbulence models. As next step, to resemble jet impingement cooling of a typical turbine guide vane, a model for an array of circular impinging jets was constructed. In the given order, these different cases are presented more thoroughly in the following sections.

3.2.1 Single slot jet model

After impinging on the flat surface, the spent air from the jet was allowed to exit at two parallel outlets. By using symmetry, simulations could be performed for only half of the domain. An illustration of the geometry and the boundaries of the model is presented in Figure 3.1. The geometry was constructed with a nozzle-to-wall spacing of $H/B = 4$ and, for discretization of the domain, three sub-regions were used. In each region, a number of divisions were specified in both x- and y-direction.

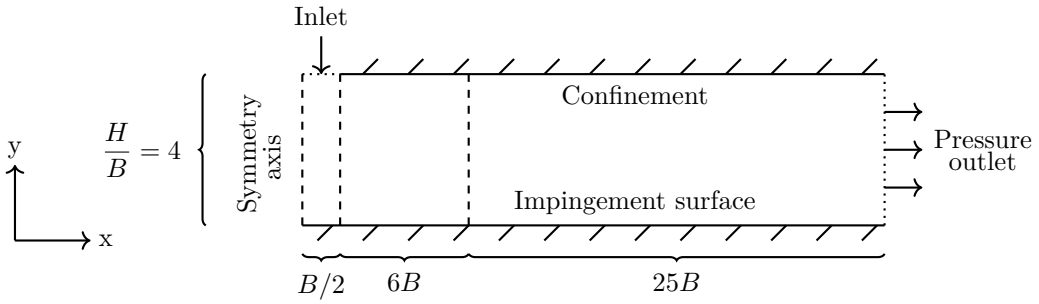

Figure 3.1: Geometry and boundaries for the model of a single impinging slot jet.

In the simulations, a jet inlet Reynolds number of $Re = 20000$ was used. Furthermore, at the jet inlet, the turbulent intensity was set to $I = 2\%$ and the turbulent length scale was given as 1.5% of the slot width i.e. $l = 0.015B$. The inlet velocity was determined from the given Reynolds number and the jet inlet width, B, using eq. 2.1. An inlet temperature of $T_{in} = 300$ K was specified. The wall temperature at the impingement surface was set to $T_w = 310$ K, whereas the temperature of the confinement was set equal to the jet inlet temperature i.e. $T_c = 300$ K. Furthermore, when calculating the resulting heat transfer coefficient and corresponding Nusselt number at the impingement surface, the inlet temperature was taken as reference temperature.

The geometry and boundary conditions for the model of the single impinging slot jet were based on information given in [15]. This article also provided the experimental data that were used for validation of the different turbulence models. The turbulence models that were evaluated for the model of the single slot jet were the realizable k-ϵ model, the standard k-ω model and the SST k-ω model. For the latter, simulations were performed both with and without a low Reynolds correction. The results from these simulations are found in Section 4.1, together with experimental data for validation.

To determine whether or not a mesh independent solution was obtained, a mesh study was performed by varying the number of division in the x-direction while keeping the divisions in y-direction constant. By comparing the obtained heat transfer coefficients at the impingement surface for the different meshes, the effect of varying the mesh resolution could be evaluated. Three meshes were studied; from the original mesh, called the base case, two alternative meshes were constructed by either refining or coarsening the mesh with regards to the number of divisions. The resulting mesh density for the different meshes can be found in Table 3.1. It should be noted that the numbering of the regions starts from inlet to outlet with respect to Figure 3.1, i.e. Region 1 corresponds to the sub-region adjacent to the symmetry axis. In Section 4.1, the results from the mesh study are presented.

Table 3.1: Mesh density used in the mesh study for the model of a single slot jet.

	Number of cells		
	Region 1	Region 2	Region 3
Base case	1650	4400	9900
Fine mesh	2200	8800	19800
Coarse mesh	1100	2200	4950

3.2.2 Model of a row of slot jets

Starting from the model that was developed for the single slot jet, the geometry was extended to include a row of five parallel jets with two outlets for exit of spent air. As for the single jet, symmetry was applied to reduce the computational effort. The distances between the jet inlets were specified as two times the jet inlet width. The boundary conditions for all inlets were the same as for the single jet. Furthermore, the choice of turbulence model was based on the results obtained from the validation of the single slot jet model.

In Figure 3.2, the geometry and the boundaries of the model for a row of jets are presented. The mesh for the domain was created using the same procedure as when constructing the mesh for the single slot jet; the difference being the number of sub-regions. Furthermore, the resolution of the mesh was determined based on the findings in the mesh study performed for the single slot jet.

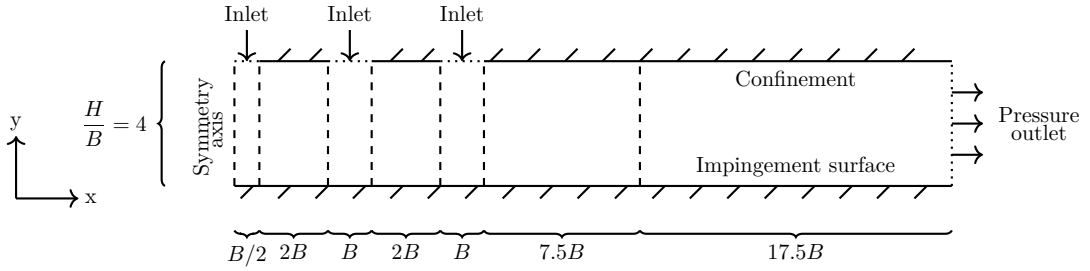

Figure 3.2: Gemetry and boundaries for the model of a row of impinging slot jets.

To check the validity of the inlet temperature as reference temperature, a study was performed to determine if a larger temperature difference between the jet inlet and the ambient fluid in the domain would influence the obtained heat transfer coefficient. This was done by varying the wall temperature at the impingement surface; a higher wall temperature will result in an increased heating of the fluid in the domain and thus a larger difference between the inlet and the ambient fluid temperature. Three different wall temperatures were tested; $T_w = 310$ K, $T_w = 400$ K and $T_w = 600$ K. The results from these simulations can be found in Section 4.2.

3.2.3 Single axisymmetric jet model

Simulations with the model of a single impinging axisymmetric jet were performed to assess the performance of different turbulence models in a similar manner as done for the single slot jet. The axisymmetric jet was assumed to exit from a long circular pipe, with a diameter D, providing a fully developed profile at the jet inlet (i.e. the pipe outlet). After impingement, the jet was allowed to spread and exit in both x- and y-direction; outlets were thus specified at the three side-boundaries of the lower domain. As for the slot jet geometries, the nozzle-to-wall spacing was set to $H/D = 4$. An illustration of the geometry and the boundaries for the model of the single axisymmetric jet is presented in Figure 3.3.

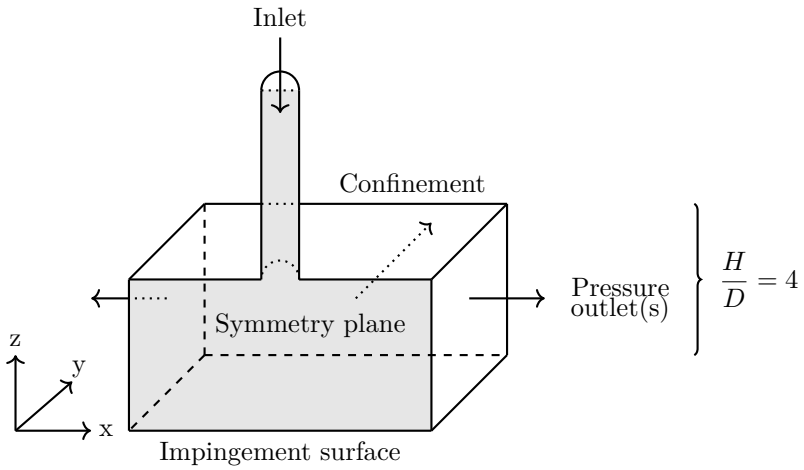

Figure 3.3: Geometry and boundaries for the model of a single impinging axisymmetric jet.

The pipe inlet was specified as a mass flow inlet and the walls of the pipe were considered adiabatic. The inlet mass flow was specified so that a Reynolds number, based on the jet velocity and the fluid properties at the outlet of the pipe, of approximately $Re = 5000$ was achieved. Data from the article [16] was used as validation. No information about the remaining boundary conditions (temperatures and pressures) were specified in the article. However, as the heat transfer coefficient at the impingement surface was assumed to mostly depend on the jet inlet Reynolds number it was assumed that these parameters could be specified arbitrary. The remaining boundary conditions were thus chosen as to resemble conditions encountered in a typical jet engine during flight and hence, due to confidentiality, they will not be presented with any further details. Simulations were performed with three different turbulence models; the standard k-ω model, the SST k-ω model (with and without low Reynolds correction) and the SST transition model. The results obtained from this validation are presented in section 4.3.

3.2.4 Model of an array of staggered jets

The model of an array of jets was constructed to resemble jet impingement cooling in a turbine guide vane. To reduce the computational cost, the model was limited to include a total of eight jet inlets. After impingement, the jets were assumed to exit through one single outlet located at the far end of the domain. To minimise the amount of backflow over the outlet boundary, the outlet was placed a certain distance away from the last jet inlet. The flow was assumed to be confined by walls on three sides; by the end-wall, the confinement surface and the impingement surface. At these surfaces, constant wall temperatures, resembling those in a typical jet engine, were specified. Translational periodicity was applied at the length of the domain, i.e. along the x-axis. An illustration of the geometry and the boundaries (excluding the jet inlets) is presented in Figure 3.4.

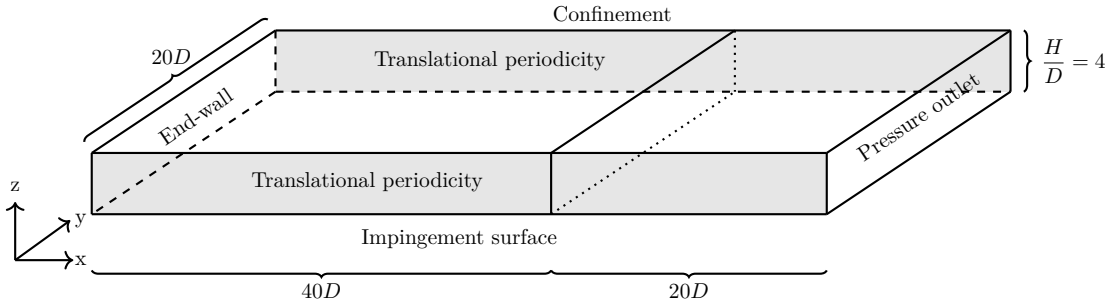

Figure 3.4: Geometry and boundaries for the model of an array of impinging jets.

At the confinement surface, a staggered distribution of the jet inlets was applied and the diameters of all inlets were set equal. Furthermore, an equal spacing between the inlets was assumed in the streamwise, x_n, and the the spanwise, y_n, direction. An illustration of the jet inlet hole configuration at the confinement surface is presented in Figure 3.5.

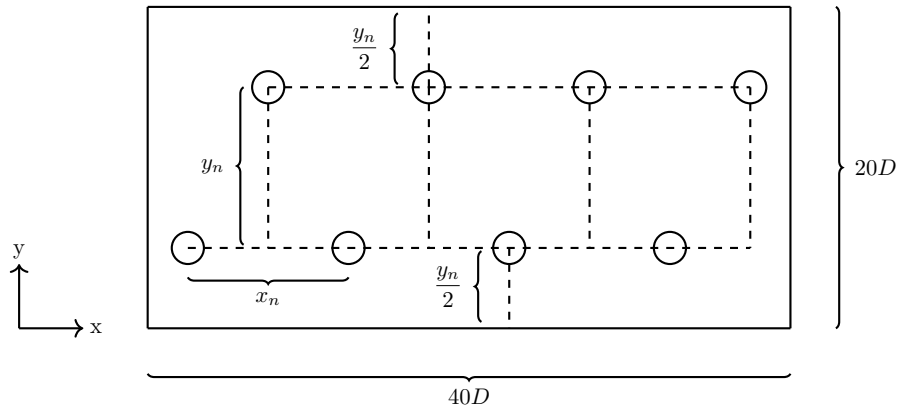

Figure 3.5: Jet inlet hole configuration used in the model for an array of jets.

Simulations were performed with two different hole spacings expressed in terms of the inlet diameter; namely $x_n = y_n = 5D$ and $10D$. For both spacings, the nozzle-to-wall distance was set to $H/D = 4$. The inlet boundary conditions were specified using values encountered in a typical jet engine during flight. For the larger spacing, $10D$, simulations were performed with two different jet inlet diameters; the smaller being one fifth of the size of the larger diameter. The results obtained with a smaller diameter, as well as a reduced spacing, are presented in Section 4.4.3. Furthermore, in the same way as done for the model of a row of slot jets, simulations were performed using three different wall temperatures at the impingement surface to check the validity of the jet inlet temperature as reference temperature. The results from these simulations are presented in Section 4.4.1.

To evaluate the heat transfer correlations presented in Section 2.6.2, mean values of the heat transfer coefficient for different Reynolds numbers were needed. The different jet inlet Reynolds numbers were achieved by varying the inlet mass flow from each hole. It should be noted that equal mass flows were specified for all inlets, i.e. the same Reynolds number were achieved at each inlet. From the heat flux at the impingement surface, area-averaged values of the heat transfer coefficient, $\overline{HTC}$, could be extracted for each Reynolds number. This was done by using ANSYS Fluent's built-in circumferential averaging function. In short, this function divides the area over which the averaging is to be done into a number of equal bands of axial (streamwise) coordinate over which the area-average of the variable is determined. This produced a number of averaged values of the heat transfer coefficient; each value corresponding to a location in the streamwise direction (i.e. a x/D-coordinate). From these area-averaged values, a mean value of the heat transfer coefficient, $\overline{\overline{HTC}}$, in the impingement region was then determined for each Reynolds number.

As a next step, the mean values of the heat transfer coefficients were used for comparing the simulated values with values obtained from the correlations developed by H. Martin and L.W. Flourschuetz (Section 2.6.2). Furthermore, for each Reynolds number, heat transfer coefficients based on a simple correlation of the form $HTC = \alpha Re^{\beta}$ were also determined. For the latter correlation, different values of the

constant α and the exponent β were evaluated. In the simplest form, the values were, for comparison, specified arbitrarily as $\alpha = 3$ and $\beta = 0.5$. Alternative values were determined in two different ways. Firstly, by rewriting the equation as $\alpha = HTC/Re^{\beta}$, the values of the exponent β could be manually tuned (or varied) so that an equal value for the constant α were obtained for each Reynolds number. This yielded a number of different values for the exponent β from which a mean value was determined and used in the final correlation, together with the value for the constant α. The second approach implied adjusting the values of α and β manually by comparing the results graphically; the obtained heat transfer coefficients were plotted against the corresponding Reynolds numbers, and the values for α and β were altered separately to obtain the best agreement, i.e. the smallest deviation, between the results. In Section 4.4.2, the results from the evaluation of the correlations are presented.

4
Results and discussion

The following chapter includes results from the simulations and the following analyses performed for the different cases presented in Section 3.2. Each case is presented separately and, in the same section, a discussion of the results and important observations is made. Decisions based on the results obtained from a previous case will be pointed out.

4.1 Single slot jet validation case

Heat transfer coefficients and Nusselt numbers at the impingement surface for the single slot jet are compared experimental data in Figure 4.1. All models can be seen to predict the highest Nusselt number at the stagnation point. At this location, the predicted values show good agreement with the experimental data; for all models, the Nusselt number in the stagnation region is within $\Delta Nu \approx 3\%$ of the experimental data. Furthermore, in agreement with the experimental data, all models predict a local minimum in the interval $1 \lesssim x/B \lesssim 3$. However, the SST k-$\omega$ model with low Reynolds correction is the only model that captures the value of this minimum. The regular SST k-ω model overestimates the value of the local minimum with $\Delta Nu \approx 11\%$, whereas the standard k-ω model and the realizable k-ϵ model overestimates this minimum with $\Delta Nu \approx 35\%$ and $\Delta Nu \approx 74\%$, respectively. It should be noted that the simulation using the realizable k-ϵ model did only converge using first order upwind scheme for spatial discretization. As the results obtained using this model are considered unreasonable when compared to the experimental data, it will not be further evaluated. Furthermore, the predicted location of the local minimum, for the experimental data occurring at $x/B \approx 2.9$, varies between the models. The standard k-ω model predicts a minimum at $x/B \approx 1.9$ whereas the SST k-ω model predicts a minimum at $x/B \approx 2.4$ ($x/B = 2.35$ with the regular SST k-ω model and $x/B = 2.42$ when applying the low Reynolds correction).

Following the local minimum, all models predict a local maximum of the Nusselt number. However, none of the compared models capture the location of this secondary peak; they all predict a maximum value at a location corresponding to a lower x/B-coordinate than the experimental data. The regular SST k-ω model underestimates the value of the secondary peak with $\Delta Nu \approx 6\%$ whereas the standard k-ω model overestimates this value with $\Delta Nu \approx 7\%$. The SST k-ω model with low

Reynolds correction overestimates the value of the secondary peak with $\Delta Nu \approx 20\%$. As no experimental data was available for the region $x/B \gtrsim 12$, no comparison between the different models has been done for this region. From these results, the regular SST k-ω model was considered most accurate in terms of agreement with experimental data and was thus used in the subsequent simulations. For the region $x/B \lesssim 12$, the SST k-ω model resulted in an area-average difference of $\approx 10\%$ compared to the experimental data.

It should be noted that, in the evaluation of the simulated results, the compared values are the minimum or the maximum value in the data set for each separate turbulence model, as well as for the experimental data. In the comparison, the simulated minimum and maximum values are thus not necessarily evaluated at the same location (i.e. the same x/B-coordinate) as the minimum or the maximum value of the experimental data. When calculating the area-averaged value, the area under graph for the k-ω model was compared to that for the experimental data. Furthermore, when calculating the deviation between the simulated and the experimental data (in percentage), the experimental data was used as a basis. The data points for the experimental data were manually read and re-created based on information given in the article "*Numerical Study of Plane and Round Impinging Jets using RANS Models*" [15].

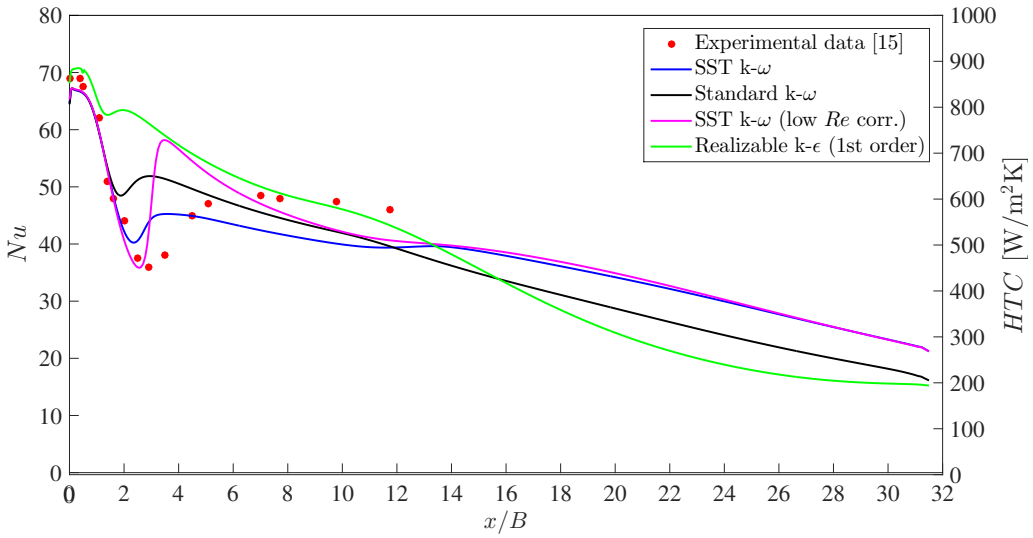

Figure 4.1: Nusselt numbers and heat transfer coefficients at the impingement surface for a single impinging slot jet. Experimental data [15] is included for comparison.

4.1.1 Mesh study

In Figure 4.2, the result from the mesh study conducted for the case with a single slot jet, using the regular SST k-ω model, is presented. It can be seen that, in the region $10 \lesssim x/B \lesssim 14$, the Nusselt numbers obtained with the coarse mesh differ slightly from those obtained with the base case and the fine mesh. In this region, the maximum deviation between the results are measured to $\Delta Nu \approx 5$ units; no larger

difference can be observed in any other region of the domain. When comparing the results obtained with the base case and the fine mesh, it can be seen that the results are closely overlapping in the entire domain. As such, it was concluded that a mesh independent solution had been obtained and that it was sufficient with a mesh resolution corresponding to that of the mesh used in the base case; any further refinements did not imply any significant differences between the results. For the subsequent cases, the meshes have thus been constructed starting from the mesh resolution used in the base case.

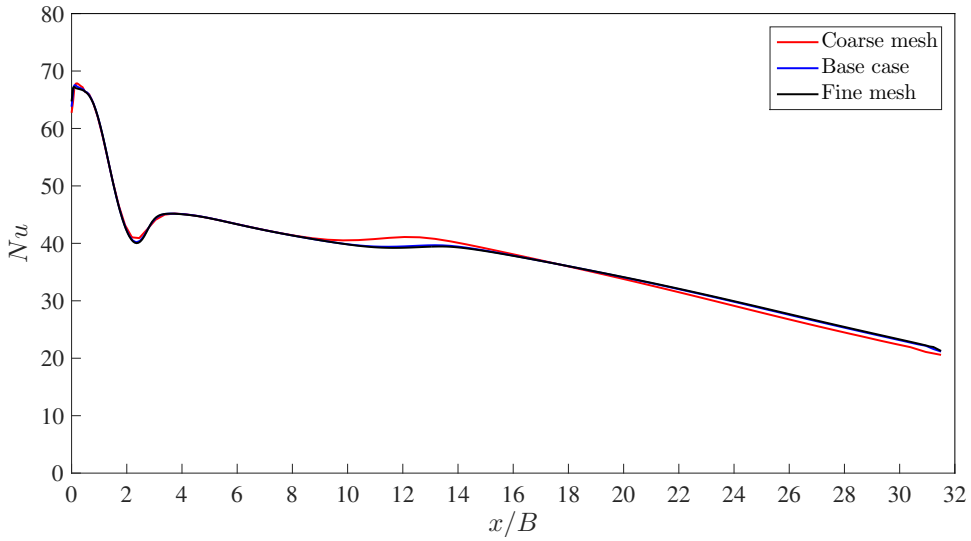

Figure 4.2: Nusselt numbers at the impingement surface for a single slot jet obtained using different mesh resolutions.

4.2 Row of impinging slot jets

Heat transfer coefficients at the impingement surface, simulated with different wall temperatures, for a row of impinging slot jets are presented in Figure 4.3. In the figure, the centre of the middle jet (here denoted as the first jet) is located at $x/B = 0$, whereas the x/B-coordinates corresponding to the centres of the second and the third jet are indicated by the two dashed lines.

When comparing the heat transfer coefficient at the location of the first jet centre with that of the single slot jet (Figure 4.1), similar values are noticed and it can be concluded that the middle jet is unaffected by the presence of the outer jets. At the location of the centres of the second and the third jet, no drastic increase nor local maximum of the heat transfer coefficient, typical for stagnation point heat transfer, can be observed. Instead, downstream of the minimum value at $x/B \approx 2$, the heat transfer coefficient can be seen to increase steadily towards a maximum value at $x/B \approx 12$ as the distance from the first jet increases; with the exception of a peak value between the second and third jet inlet. Downstream of the maximum, the heat transfer coefficient is decreasing with increasing x/B-value.

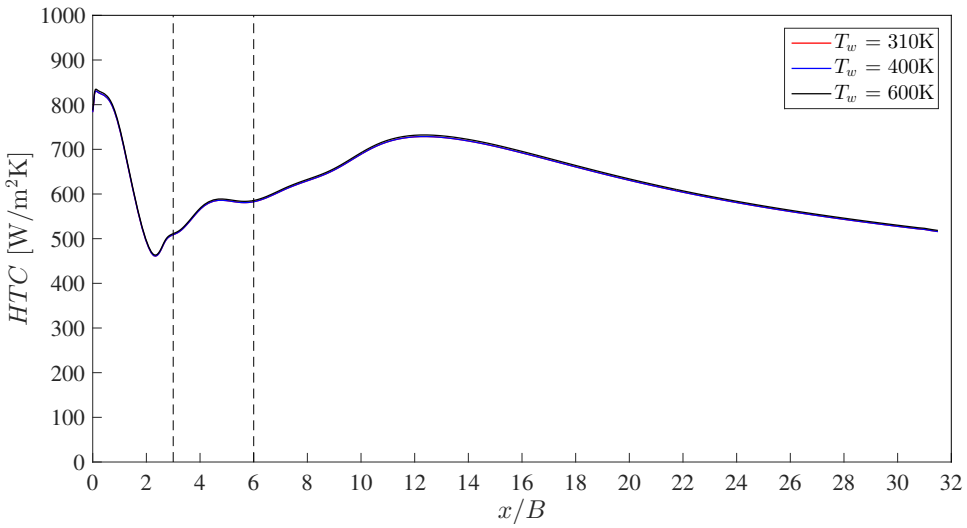

Figure 4.3: Heat transfer coefficients for different wall temperatures at the impingement surface for a row of slot jets.

The heat transfer coefficients presented in Figure 4.3 were calculated using the jet inlet temperature as reference temperature. To validate this choice of reference temperature, the wall temperature at the impingement surface was varied in order to determine if a larger temperature gradient between the jet exit temperature and temperature of the ambient fluid would influence the prediction of the heat transfer coefficient. As can be seen by the results in Figure 4.3, this variation resulted in a barley noticeable difference between the cases. When compared to the values for the lowest temperature, the difference between the heat transfer coefficients was observed to increase with increasing wall temperature. When comparing the heat transfer coefficient obtained with a wall temperature of $T_w = 310$ K with that for a wall temperature of $T_w = 600$ K, the largest difference in the domain could be determined to $\Delta HTC \approx 4$ W/m^{2}K.

An explanation behind the heat transfer behaviour that is observed in Figure 4.3 may be given by studying the contour plot of the normalised velocity in the domain presented in Figure 4.4. It is observed that no large-scale mixing of the three jet streams occur; the second and third jet stream do not reach the impingement surface, they are simply adding their mass flow to the main stream. This effect could be caused by the simplification of modelling the system in 2D. The first jet impinges on the impingement surface, unaffected by the two outer jets, resulting in a heat transfer coefficient corresponding to that of the single jet. After turning, the flow from the first jet spreads along the impingement surface. As the flow is limited to spread only in the streamwise direction, the flow in the wall jet region is pressed against the wall by the addition of the mass flow from the second and third jet. This causes a reduction of the cross-sectional area of the flow in the wall jet region and hence an acceleration of the flow which enhances the heat transfer rate in these regions. Downstream of the stagnation point of the first jet, the largest value of the heat transfer coefficient is obtained at the same x/B-coordinate at which the velocity magnitude can be seen to reach its highest value. Moving downstream from this

maximum, the cross-sectional area of the flow is increasing; causing a deceleration of the flow in the wall jet region and hence a reduction of the heat transfer rate.

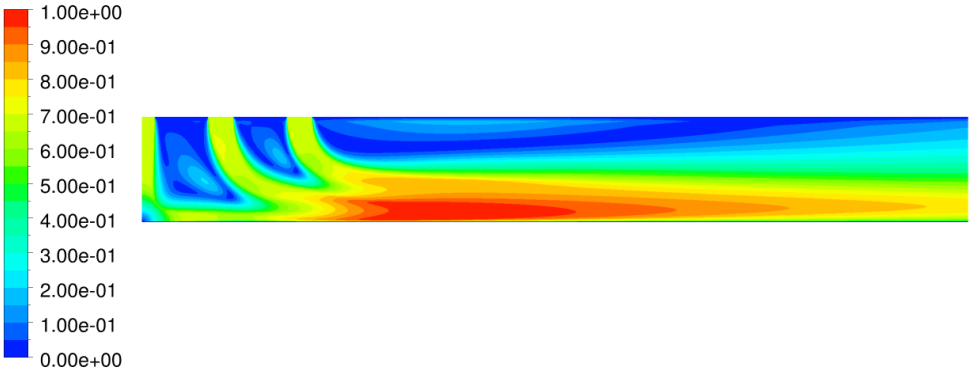

Figure 4.4: Normalised velocity along the streamwise direction for a row of impinging slot jets.

4.3 Single axisymmetric jet validation case

In Figure 4.5, the Nusselt numbers at the impingement surface for the single axisymmetric jet are presented together with experimental data. At the x-axis, the non-dimensional distance from stagnation point ($x/D = 0$) is shown. As an iterative manner of varying the mass flow at the jet inlet was needed to obtain accurate Reynolds numbers in each simulation, the Reynolds numbers used in the comparison of the different models are not completely in agreement with experimental data (i.e. $Re = 5000$). However, these differences were considered negligible and it was assumed that the results from the simulations were comparable with experimental data.

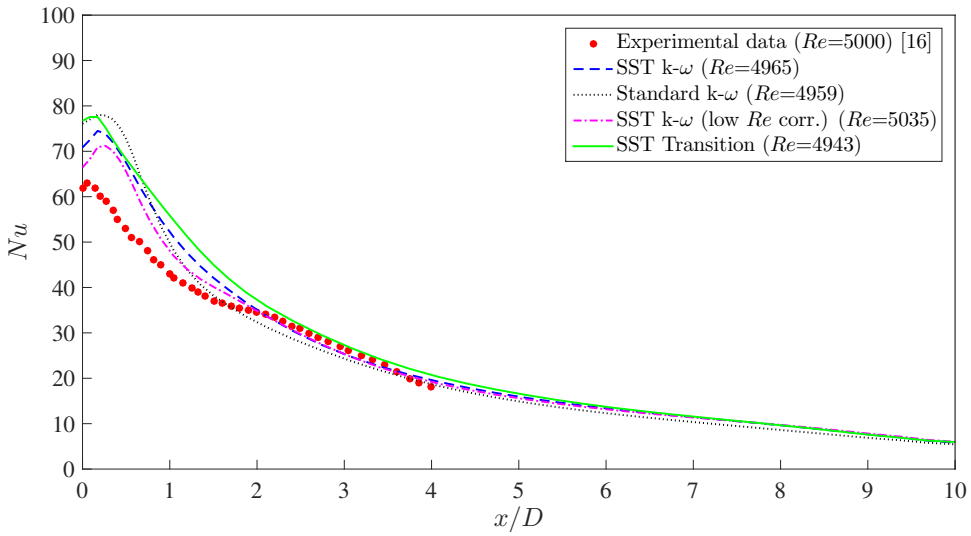

Figure 4.5: Nusselt numbers at the impingement surface for a single axisymmetric jet. Experimental data [16] is included for comparison.

In Figure 4.5, it can be seen that the maximum Nusselt numbers occur at a small distance from the stagnation point; this behaviour is noticed both for the experimental data and the simulated values. However, the simulated values seem to overestimate the difference between the Nusselt number at the stagnation point and at this outer maximum. The offset of the maximum Nusselt number from the stagnation point might be explained with the same theories as used for a single unconfined jet; as the fluid accelerates out from the stagnation region, the thickness of the boundary layer at this location is reduced and the heat transfer rate enhanced. This explanation is accompanied by a theory stating that the heat transfer rate at this location is further enhanced due to turbulence generated in the shear layer [17]. Why a similar behaviour was not observed for the single slot jet has not been evaluated. Following this maximum value, the experimentally determined Nusselt number is decreasing up until $x/D \approx 2$. At this location, the Nusselt number starts to increase towards a secondary, relatively small local maximum. After the secondary peak, the Nusselt number is again decreasing as the distance from the stagnation point increases.

When looking at the results obtained from simulations with the different turbulence models, it can be seen that none of the models are able to capture this secondary peak; for all models, the Nusselt number is continuously decreasing as the distance from the stagnation region increases. Why this secondary peak is observed has not been fully understood but it has, by some authors, been attributed to a transition from laminar to turbulent flow in the boundary layer [11, 17]. A secondary peak was observed also for the experimental data for the single slot jet (Figure 4.1). However, for the single slot jet the results predicted by the different turbulence models showed an increased Nusselt number in the same region as where the secondary peak was observed for the experimental data. If the secondary peak can be described with a transition of the flow in the boundary layer, a further explanation as to why the models do not predict this peak for the axisymmetric jets could be the lower Reynolds number used in the simulations. For the single slot jet, a jet inlet Reynolds number of $Re = 20000$ was given, whereas for the single axisymmetric jet, a value of $Re = 5000$ was used. For the lower Reynolds number, the amplitude of the fluctuations might be to small to be predicted by the turbulence models with the current mesh.

The largest differences between the experimental data and the simulated values are observed in the region closest to the stagnation point. In this region, the regular SST $k-\omega$ model overestimates the maximum Nusselt number with $\Delta Nu \approx 18\%$; with the low Reynolds correction this is reduced to $\Delta Nu \approx 13\%$. The standard $k-\omega$ model and the SST transition model overestimates the maximum Nusselt number with $\Delta Nu \approx 24\%$ and $\Delta Nu \approx 23\%$, respectively. Thus, for the case with a single axisymmetric jet, the results obtained with the SST $k-\omega$ model with low Reynolds correction were considered most accurate. However, as the same model overestimated the heat transfer coefficient for the single slot jet, for which the Reynolds number was set to a higher value, and as the performance of the different models was approximately the same for the single axisymmetric jet, the regular SST $k-\omega$ model was, altogether, deemed most accurate and stable. Thus, in the following cases where the Reynolds number have been varied to cover a larger interval, the

regular SST $k-\omega$ model has been used. For the region $x/B \lesssim 4$, the SST k-ω model resulted in an area-average difference of $\approx 15\%$ compared to the experimental data.

4.4 Array of staggered jets

The results acquired from simulations with the array of jets have been divided into four different parts; effect of wall temperature variation, evaluation of heat transfer correlations, jet interaction and crossflow and, lastly, scaling of the model. In the following sections, these different parts will be presented in given order.

4.4.1 Effect of wall temperature variation

Simulations with different wall temperatures at the impingement surface were performed with a hole spacing of $x_n = y_n = 10D$. For each wall temperature, two jet inlet Reynolds numbers were evaluated. Area-averaged values of the heat transfer coefficient at the impingement surface were extracted using ANSYS Fluent's built-in circumferential averaging function as mentioned in Section 3.2.4. In Figure 4.6, the resulting heat transfer coefficients are plotted against the corresponding non-dimensional distance from the end-wall (located at $x/D = 0$). The upper values in Figure 4.6 were obtained with $Re \approx 16400$, whereas the lower values were obtained using a jet inlet Reynolds number of $Re \approx 3250$. From the area-average values, mean deviations between the results obtained with the different wall temperatures were determined. Due to possible end-wall effects, the mean values were determined for the interval limited by the dashed lines in the figure. In this interval, the predicted results are assumed to be independent of possible effects caused by the end-wall. This procedure has been used in the following parts of the project as well.

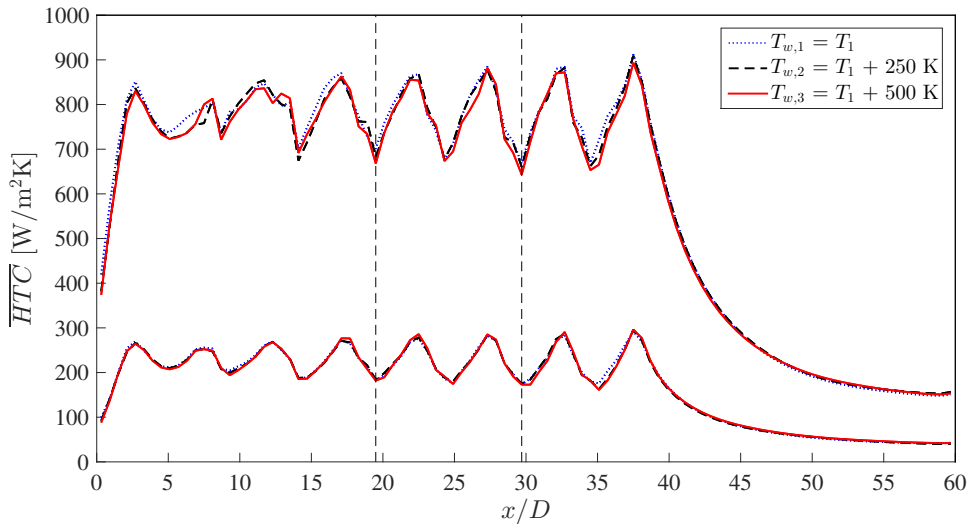

Figure 4.6: Area-averaged heat transfer coefficients at the impingement surface for an array of jets with varying wall temperatures.

For a lower Reynolds number, $Re \approx 3250$, an increase of the wall temperature of $\Delta T_w = 250$ K resulted in a average deviation between the predicted heat transfer coefficients of $\Delta\overline{\overline{HTC}} \approx 0.4\%$. When increasing the wall temperature further, resulting in a temperature difference of $\Delta T_w = 500$ K, this deviation increased $\Delta\overline{\overline{HTC}} \approx 0.8\%$. The same trend was observed for a higher Reynolds number, $Re \approx 16400$. The largest temperature difference for this Reynolds number resulted in an average deviation of $\Delta\overline{\overline{HTC}} \approx 1.7\%$. These values were, however, considered negligible and the effect of varying the wall temperature was thus assumed to be minor for the tested temperature interval. In the following simulations, the inlet temperature has thus been used as reference temperature. As the average deviation was seen to increase with increasing wall temperature, the use of another reference temperature might, however, be necessary if larger temperature differences are present in the domain.

4.4.2 Evaluation of heat transfer correlations

With the larger hole spacing, $10D$, and a wall temperature corresponding to $T_{w,1}$, different jet inlet Reynolds numbers were achieved by varying the inlet mass flow to each hole. For each Reynolds number, area-averaged heat transfer coefficients were determined and plotted against the corresponding spatial coordinate; the result is presented in Figure 4.7. The contribution of the high heat transfer rate at the stagnation regions can be seen as peak values in the figure.

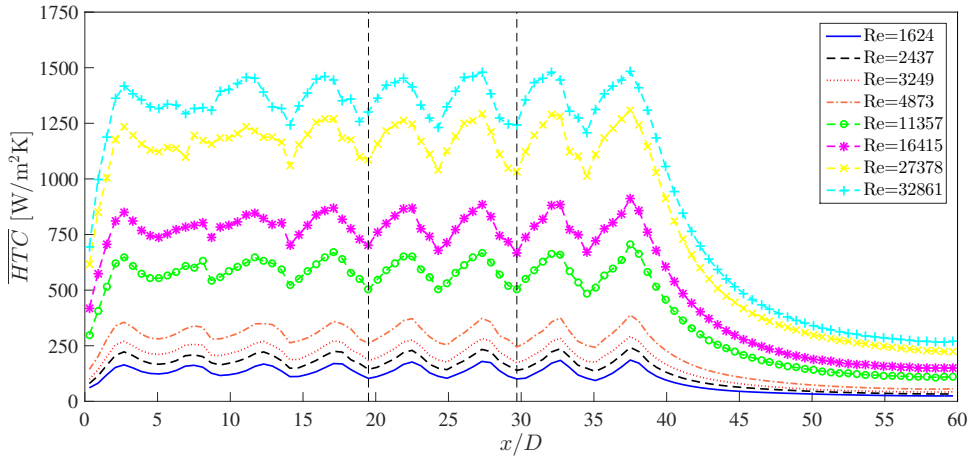

Figure 4.7: Area-averaged heat transfer coefficients at the impingement surface for an array of jets using various jet inlet Reynolds numbers.

Eight different Reynolds numbers in the range $1600 \lesssim Re \lesssim 32900$ were evaluated as presented in the legend of Figure 4.7. The validity of the correlation presented by H. Martin was, however, said to be limited to jet inlet Reynolds numbers in the interval $2000 \leq Re \leq 100000$ (Appendix A); this includes all but the lowest Reynolds number used in the simulations. The values used for the remaining parameters, for which a range of validity was specified, were $H/D = 4$ and $A_r = 0.0079$. These values were thus within the specified range presented in Appendix A. Furthermore, the Reynolds numbers used when developing the correlation by L.W. Florschuetz et al.

ranged from $5000 \lesssim Re \lesssim 50000$ [14]. As such, when comparing the simulated values for the mean heat transfer coefficient with those obtained with the correlations, only values for $Re > 5000$ have been included; these are indicated as red dots in Figure 4.8. In Figure 4.8, heat transfer coefficients obtained from calculations using the two correlations derived by H. Martin and L.W. Flourschuetz et al. (Section 2.6.2) are also included, together with values obtained from a correlation of the form $HTC = \alpha Re^{\beta}$ (Section 3.2.4). For the latter, the values of the constants α and the β, that where obtained from either tuning or from graphical comparison, are included in the legend to the figure.

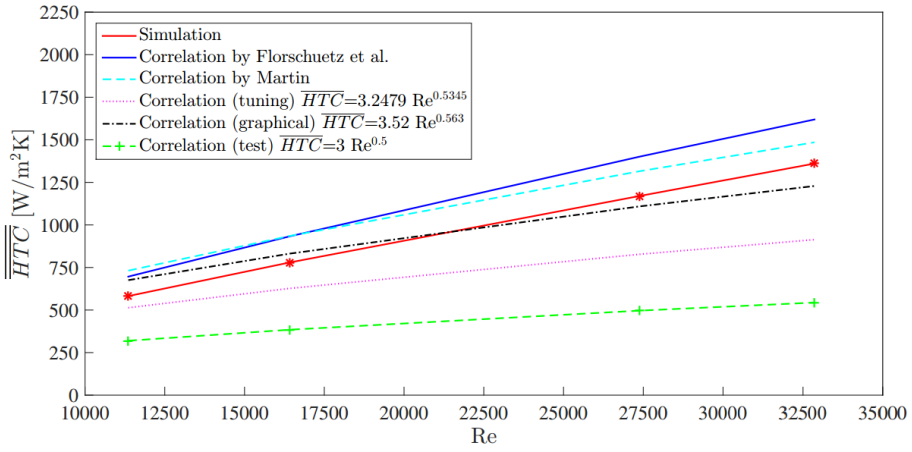

Figure 4.8: Mean value of area-averaged heat transfer coefficients obtained from simulations as well as heat transfer correlations for an array of jets.

Looking at the results obtained using the simple correlation with the values $\alpha = 3$ and $\beta = 0.5$ (green line), it can be seen that the correlation highly underestimates the heat transfer coefficient for all Reynolds number. Furthermore, the difference between the simulated and the correlated values is observed to increase with increasing Reynolds number. The same behaviour is observed when using manually tuned values for α and β (pink line). However, using the tuned values gives higher heat transfer coefficients for all Reynolds number when compared to using the arbitrarily determined values. Furthermore, assuming a strictly linear behaviour, a larger slope of the line, i.e. a higher dependence on the Reynolds number, is observed when using the tuned values. With the graphically determined values for α and β, the correlation overestimates the heat transfer coefficient in the lower interval whereas it underestimates the values for higher Reynolds numbers. Comparing the three different forms of the simple correlation, it is with the graphically determined values that the slope of the line for the predicted values and the values for the Nusselt number show best agreement with the simulations. The difference is however still relatively large and can be seen to increase outside the evaluated range of Reynolds numbers. It is thus concluded that it is not enough with a correlation of this simple form to describe the behaviour of the heat transfer at the impingement surface.

The correlation by L.W. Flourschuetz et al. (blue line) overestimates the heat transfer coefficient and the difference compared to the simulated values can be seen to increase for higher Reynolds numbers. Compared to the simulated values, this

correlation results in an average deviation of $\Delta\overline{\overline{HTC}} \approx 15\%$. The correlation recommended by H. Martin also overestimates the values for all Reynolds numbers (cyan line). Compared to the correlation by L.W. Flourschuetz et al., the average deviation for the evaluated range of Reynolds number is, however, smaller for the correlation by H. Martin, $\Delta\overline{\overline{HTC}} \approx 15\%$. Furthermore, for the H. Martin correlation, the difference compared to the simulated values is decreasing for higher Reynolds numbers. Compared to the simulated values, the correlation by H. Martin result in a similar dependence of the Reynolds number; the difference between the results is observed to mainly be in the form of an offset of the values. The difference between the slopes for the simulated values and the values obtained with the H. Martin correlation is relatively small; the simulated values has a slope of 0.036, whereas, for the correlated values, this is measured to 0.035. This can be compared to the same value for the correlation by Florschuetz et al. which was measured to 0.043; for the different variants of the simple correlation, this difference was even larger.

The results presented above suggest that the main effect influencing the heat transfer in the jet array, apart from the jet inlet Reynolds number, corresponds to the additional parameters included in the correlation recommended by Martin; i.e. the non-dimensional nozzle-to-wall distance and the spanwise and streamwise hole spacing. In the H. Martin correlation, the latter are incorporated in the variable A_r. The effect of crossflow in the array does not seem to be as large as predicted by the correlation by Florschuetz et al. Depending on the required level of certainty, it is thus deemed possible to use the correlation recommended by Martin to get an estimate of the mean heat transfer coefficient at the impingement surface for the evaluated range of Reynolds numbers. However, as both extended correlations (by Martin and Florschuetz et al., respectively) have been developed empirically for certain conditions, there will always be uncertainties concerning the application of these correlations in other systems.

4.4.3 Jet interaction and crossflow

In Figure 4.9, the normalised velocity at the streamwise cross-sectional area at the centre of one of the jet rows in the array is presented. In the simulation, a Reynolds number of $Re \approx 4800$ and a hole spacing of $x_n = y_n = 10D$ was used. Looking at the first jet in the row, an interaction with the ambient fluid can be seen to result in a widening of the velocity profile caused by shearing at the edges of the jet. An effect of interaction between the jets is noticed after the jets have impinged on the impingement surface. In the middle of two neighbouring jets, the wall jets of the two adjacent jets collide resulting in a region of reduced velocity. Furthermore, the collision of the wall jets forces the flow to change direction which introduces a "fountain effect". Moving towards the end of the jet row, the effect of interaction and crossflow can be seen to increase. The velocity profiles of the jets are becoming more and more asymmetrical and for the last jet, the stagnation point can also seen to be shifted slightly towards the outlet of the domain, whereas for the upstream jets, the stagnation point is located directly below the centre of each jet inlet. Furthermore,

as the last jet approaches the impingement surface, the cross-sectional area of the high-velocity region (or the core region) is seen to be decreasing more rapidly than for the preceding jets.

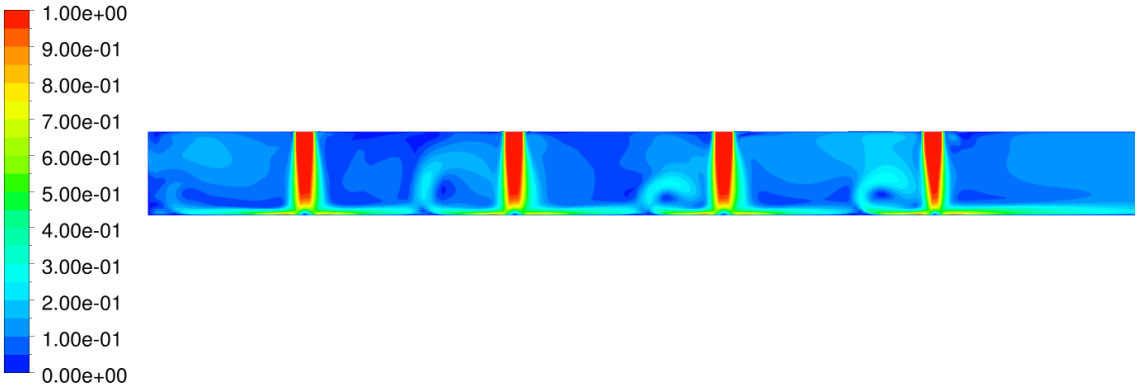

Figure 4.9: Normalized velocity evaluated at the streamwise cross-sectional area at the jet centre in the array.

In Figure 4.10, the local Nusselt number at the impingement surface, corresponding to the row of jets shown in Figure 4.9, is presented. As for the single axisymmetric jet, each stagnation point corresponds to a local minimum of the Nusselt number whereas the maximum Nusselt numbers are obtained at a small offset from these points. Furthermore, at the location of the collision of the wall jets, local maximums are present. When comparing the maximum Nusselt numbers for the array (Figure 4.10) with the maximum value predicted for the single axisymmetric jet (Figure 4.5), it can be seen that the maximum values obtained for the array do not reach the same levels. Furthermore, when comparing the Nusselt number of the first and the last jet in the array, a small decrease is observed; the maximum Nusselt for the first jet is measured to $Nu \approx 58$, compared to $Nu \approx 56$ for the last jet.

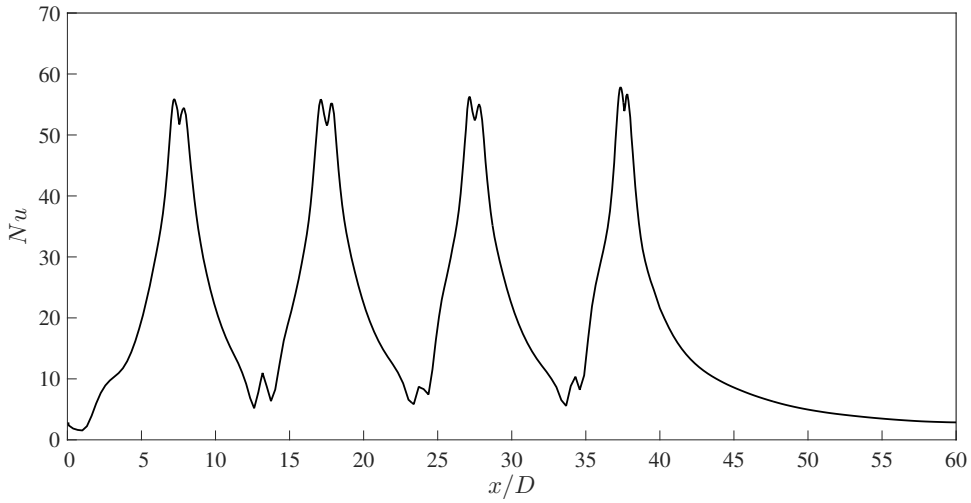

Figure 4.10: Local Nusselt number at the impingement surface for the jet centre in the array.

Depending on the hole spacing, when compared to a single jet, the interaction between the jets before impingement, and hence the increased shearing at the edges of the jets, causes the velocity of the jets in the array to decrease more rapidly and increases the entrainment of surrounding fluid [17]. This could be further enhanced to due the "fountain effect" introduced above; an interaction between the flow in the fountain and the jet could increase the shearing and thus reduce the jet velocity and the corresponding heat transfer rate [11]. These differences could explain the deviation between the Nusselt numbers observed for the two cases, however, in this case, the main cause for the different results is assumed to be due the different velocity profiles that were applied. For the single axisymmetric jet, a fully developed profile was used, whereas in the jet array, a uniform velocity profile was specified at each inlet. With the fully developed profile, the velocity in the core region of the jet reaches higher values resulting in an increased heat transfer rate when impinging on the surface [18]. It should be noted that there is a small difference between the jet inlet Reynolds number used in the two cases that also influences the results.

The effect of interaction between the jets as well as crossflow from upstream jets can also be studied by looking at the contour plot of the normalised heat flux evaluated at the impingement surface in Figure 4.11. It should be mentioned that the normalised velocity (Figure 4.9) and the Nusselt number (Figure 4.10) here belongs to the upper jet row.

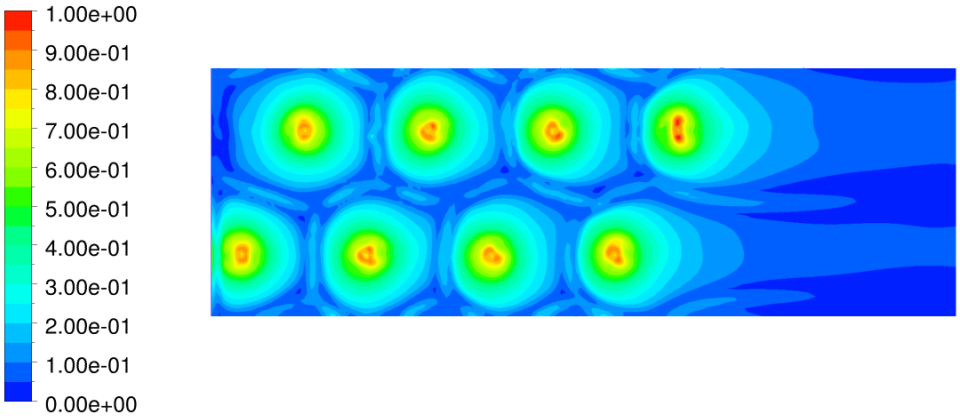

Figure 4.11: Normalised heat flux at the impingement surface for an array of jets.

For the first jet in the upper row, for which a symmetrical velocity profile was observed (Figure 4.9), a symmetrical behaviour is also observed for the corresponding heat flux. However, when looking at the last jet in the row, a deflection of the profile is noticed; this is especially clear when looking at the stagnation point. The high heat flux observed at this point, corresponding to the high Nusselt number seen in Figure 4.10, could possibly be explained by the narrowing of the core velocity region of the last jet noticed in Figure 4.9. The crossflow from upstream jets results in a concentration of mass flow of the last jet to a smaller surface area than observed for the previous jets in the array which, in turn, enhances the heat transfer at this location. Altogether, these results indicate that there is an effect of crossflow on the heat transfer in the jet array. However, in agreement with the results presented

in Section 4.4.2, the effect can be seen to be minor. As the model of the jet array was limited to include only four jets in the streamwise direction, and as the effect of crossflow is observed to increase further downstream, it might, however, be of importance to consider this effect for larger arrays.

4.4.4 Scaling of the model

In the following sections, the results of varying either the spacing between the inlets or the jet inlet diameter are presented and discussed.

4.4.4.1 Reduced hole spacing

With a Reynolds number of $Re \approx 3250$ and the larger jet inlet diameter, the spacing between the inlets was reduced from $10D$ to $5D$ in both streamwise and spanwise direction. As the inlet diameter and the inlet mass flow to each hole were kept constant, this resulted in an equal Reynolds number but a higher mass flow per impingement area. The resulting area-averaged heat transfer coefficient is given by the blue line in Figure 4.12. From these values, the mean heat transfer coefficient was determined to $\overline{\overline{HTC}} \approx 426$ W/m^{2}K. As a next step, it was assumed that the total mass flow to the guide vane, and thus the total mass flow per impingement area (or mass flux), was limited to a maximum value. The maximum value corresponded to the inlet mass flow used in the model with a larger spacing and a Reynolds number of $Re \approx 3250$. In the model with reduced spacing, the inlet mass flow was thus reduced so that an equal mass flux was achieved for the smaller and the larger model. As the mass flow was reduced, this also resulted in a reduced jet inlet Reynolds number. In Figure 4.12, the area-averaged heat transfer coefficient obtained from this simulation is given by the black line. The corresponding mean value for the heat transfer coefficient was determined to $\overline{HTC} \approx 177$ W/m^{2}K.

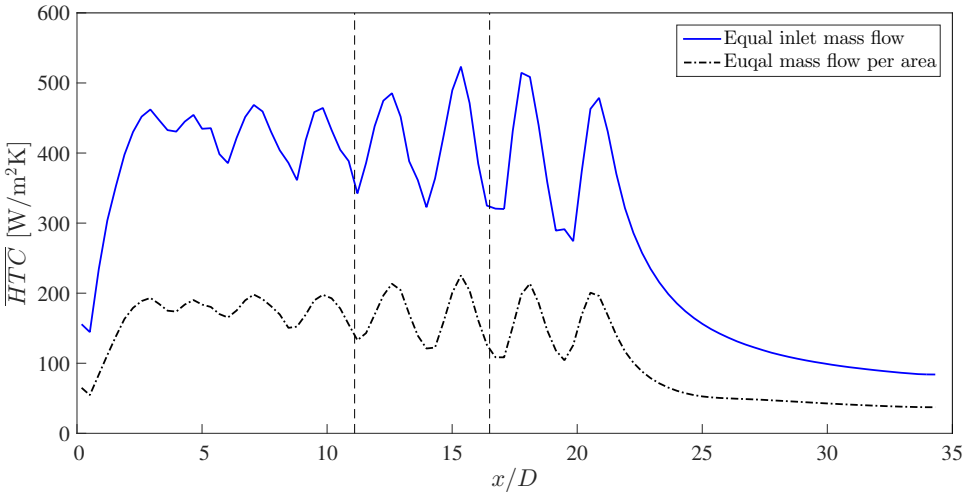

Figure 4.12: Area-averaged heat transfer coefficients for a hole spacing of $x_n = y_n = 5D$.

For the larger spacing, $10D$, a Reynolds number of $Re \approx 3250$ resulted in a mean heat transfer coefficient of $\overline{\overline{HTC}} \approx 224$ W/m^{2}K (Figure 4.7). Compared to this value, it can be seen that reducing the hole spacing results in a higher value of the

mean heat transfer coefficient at the impingement surface ($\overline{\overline{HTC}} \approx 426$ W/m^{2}K.). This is expected as a larger part of the impingement surface for the model with a larger spacing is occupied by wall jet regions, with low heat transfer rates, than for the model with reduced spacing. Reducing the spacing thus results in an increased percentage of the area corresponding to impingement zones, with high heat transfer rates, and the area-averaged heat transfer coefficient is thus increased.

On the other hand, when comparing the vales obtained for the models with equal mass flux, a higher mean heat transfer coefficient is observed with the larger hole spacing. As the Reynolds number is reduced for the model with smaller spacing, not as high local heat transfer rates are obtained as for the model with larger spacing. However, at the same time, also the size of the impingement area, over which the averaging is done, is reduced. As a higher mean heat transfer coefficient still is obtained with the larger spacing, this indicates that additional effects that reduce the heat transfer rate, e.g. increased jet-to-jet interaction, are present in the model with reduced spacing. For a limited mass flow, the most efficient hole spacing, in terms of highest area-averaged heat transfer coefficient, was thus a spacing of $10D$.

4.4.4.2 Reduced jet inlet diameter

In the model of the jet array, the inlet diameter was reduced to one fifth of the original value; however, still with a spacing of $x_n = y_n = 10D$ (expressed in terms of the smaller diameter). In Figure 4.13, area-averaged heat transfer coefficients obtained from simulations with the reduced diameter are presented for three different Reynolds numbers.

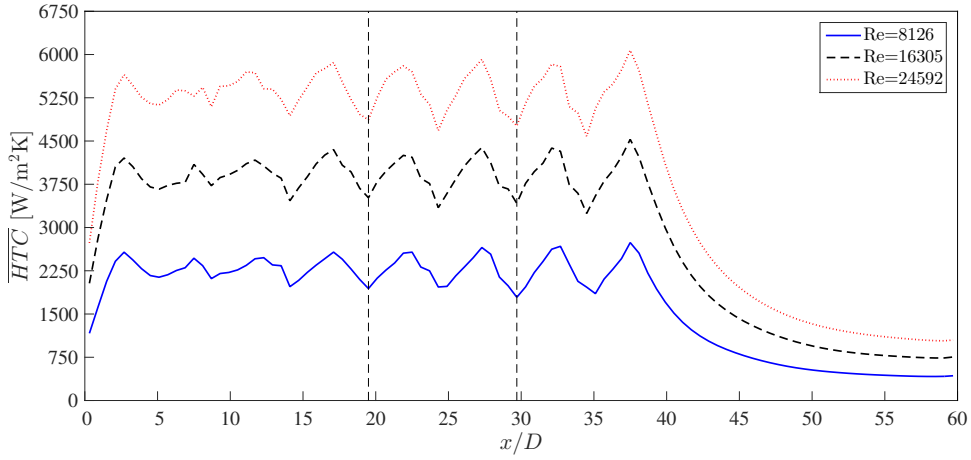

Figure 4.13: Area-averaged heat transfer coefficient for an array of jets with a reduced inlet diameter.

When comparing these values with those obtained for the jet array with larger diameter (Figure 4.7), it can be seen that with the smaller diameter, much higher heat transfer coefficients are obtained. This difference is caused by the higher velocity of the jets needed to obtained similar values for the Reynolds number in the model with reduced diameter. For a Reynolds number of $Re \approx 16000$, the mean value for the heat transfer coefficient was, for the model with larger diameter, measured to

$\overline{\overline{HTC}} \approx 780$ W/m^{2}K. For the smaller diameter, a value of $\overline{\overline{HTC}} \approx 3880$ W/m^{2}K was observed; this corresponds to an increase of approximately five times.

From the mean heat transfer coefficients, corresponding to a Reynolds number of $Re \approx 16000$, Nusselt numbers were calculated for both the larger and the smaller model. As the same jet inlet temperature was used in both models, equal values of the thermal conductivity of the fluid were obtained. Furthermore, as an ratio of 1/5 between the smaller and the larger diameter was used, the same ratio as obtained between the corresponding heat transfer coefficients, an equal value of the Nusselt number thus obtained for both models. This implies that it is possible to assume a uniform behaviour of the non-dimensional heat transfer parameters when either increasing or decreasing the size the diameter, as long as equal conditions, e.g. Reynolds number and non-dimensional geometry parameters, are used.

5

Conclusions and future work

Modeling of more than a single slot jet in 2D was seen to result in unwanted effects. For the jet array, it is possible to assume uniformity between non-dimensional parameters when scaling up or down the system. For the temperature interval that was used, varying the wall temperature at the impingement surface was observed to have minor effect on the prediction of heat transfer coefficients. It is thus concluded that it is possible to use the jet inlet temperature as reference temperature and obtain independent results. However, as the deviations between the simulations were observed to increase for larger temperature differences, it is recommended to evaluate the use of other reference temperatures if predictions for higher temperature levels are requested.

It was observed that a simple correlation of the form $HTC = \alpha Re^{\beta}$ is inadequate of describing heat transfer in the jet array; additional parameters need to be considered. The spacing between the inlets was considered as an important parameter, whereas the presence of crossflow had minor effect on the heat transfer rate. However, if a larger array (including more jets) is to be studied, the latter might become relevant. The correlation that showed best agreement with the predicted data was the correlation recommended by Martin [13]. This correlation is considered sufficient for acquiring an approximate value of the average heat transfer coefficient.

To gain a more in-depth description of heat transfer due to jet impingement cooling in the guide vane, transient simulations might be performed to evaluate the assumption of a steady-state behaviour. Furthermore, the possible effects of transitional boundary-layer flow have only been touched upon and require further analyses.

Bibliography

[1] Saravanamuttoo, H.I.H., Rogers, G.F.C., Cohen, H. and Straznicky, P.V. *Gas Turbine Theory* (6th ed.) Harlow, Pearson Education Limited, 2009.

[2] Xu, L., Bo, S., Hongde, Y. and Lei, W. *Evolution of Rolls-Royce air-cooled turbine blades and feature analysis*. Procedia Engineering, Vol. 99, p. 1482-–1491, 2015.

[3] Welty, J., Wicks, C.E., Rorrer, G.L. and Wilson R.E. *Fundamentals of Momentum, Heat and Mass Transfer* (5th ed.) Hoboken, John Wiley & Sons Inc., 2008.

[4] Andersson, B., Andersson, R., Håkansson, L., Mortensen, M., Sudiyo R. and van Wachem, B. *Computational Fluid Dynamics for Engineers* (11th ed.) Cambridge, Cambridge University Press, 2015.

[5] Sundén, B. *Introduction to Heat Transfer*. Boston, WIT Press, 2012.

[6] Blazek, J. *Computational Fluid Dynamics - Principles and Applications* (3rd ed.) Oxford, Butterworth-Heinemann, 2015.

[7] ANSYS, Inc. *ANSYS Fluent 15.0 User's guide*. Canonsburg, ANSYS Inc., 2013.

[8] Aainsqatsi, K. (own photography) Distributed under a CC BY-SA 3.0 license (http://creativecommons.org/licenses/by-sa/3.0) via Wikimedia Commons. Available at `https://commons.wikimedia.org/w/index.php?curid=4008470` [Accessed 2015-04-27]

[9] Yahya, S.M *Turbines, Compressors and Fans* (4th ed.) New Dehli, McGraw-Hill Education Private Limited, 2011.

[10] Han, J-C., Dutta, S. and Ekkad, S. *Gas Turbine Heat Transfer and Cooling Technology* (2nd ed.) Boca Raton, CRC Press, 2012

[11] Zuckerman, N. and Lior, N. *Jet Impingement Heat Transfer: Physics, Correlations, and Numerical Modeling*. Advances in Heat Transfer, Vol. 39, 565–631, 2006.

[12] Taylor, R. *Heat Transfer Phenomena in Gas Turbines* ASME International Gas Turbine Conference and Products Show; No. 80-GT-172, Vol. 1B: General, 1980.

[13] Holger, M. *Heat and mass transfer between impinging jets and solid surfaces*. Advances in heat transfer, Vol. 13, p. 1–60, 1977.

[14] Florschuetz, L.W., Truman, C.R. and Metzger, D.E. *Jet array impingement with crossflow - correlation of streamwise resolved flow and heat transfer distributions*. Washington, D.C., National Aeronautics and Space Administration, Scientific and Technical Information Branch, 1981.

[15] Jaramillo, J.E., Pérez-Segarra, C.D., Rodriguez, I. and Oliva, A. *Numerical Study of Plane and Round Impinging Jets using RANS Models*. Numerical Heat Transfer, Part B: Fundamentals, Vol. 54, No. 3, p. 213–237, 2008.

[16] Lee, L. and Lee, S-J. *Stagnation region heat transfer of a turbulent axisymmetric jet impingement*. Experimental heat transfer, Vol. 12, No. 2, p. 137–156, 1999.

[17] Huber, A.M. and Viskanta, R. *Effect of jet-jet spacing on convective heat transfer to confined, impinging arrays of axisymmetric air jets*. International Journal of Mass Transfer, Vol. 37, No. 18, p. 2859–2869, 1994.

[18] Bovo, M. and Davidson, L. *On the Numerical Modeling of Impinging Jets Heat Transfer - A Practical Approach*. Numerical Heat Transfer, Part A: Applications, Vol. 64, No. 4, p. 290–316, 2013.

A

Additional correlation information

The following sections include additional information regarding the correlations recommended by H. Martin [13] and Florschuetz et al. [14] (Section 2.6.2).

A.1 Range of validity

The range of validity for the correlation recommended by H. Martin [13] is given by the following parameter intervals:

$$2000 \leq Re \leq 100\,000$$
$$0.004 \leq A_r \leq 0.04$$
$$2 \leq H/D \leq 12$$

A.2 Correlation constants

In Table A.1, values for the constants K_1, K_2, m and n to be used in eq. 2.6.2 are presented.

Table A.1: Correlation constants for an array of staggered jets. [14]

	C	n_x	n_y	n_z
K_1	1.87	-0.771	-0.999	-0.257
m	0.571	0.028	0.092	0.039
K_2	1.03	-0.243	-0.307	0.059
n	0.442	0.098	-0.003	0.304